# Chapter VIII
# Mg and Sr Co-Doped Ceria and its Nanocomposites

This chapter contains two sections. Section 1 describes the effect of co-doping of $Mg^{2+}$ and $Sr^{2+}$ on the crystal structure, morphology and electrical properties of ceria. The composition which shows the highest conductivity in this system has been chosen for the nanocomposites. Section 2 focuses on the effect of concentration of binary carbonates mixture [$(Li_{0.52}Na_{0.48})_2CO_3)$] on the phases, thermal, microstructural and electrical properties of $Mg^{2+}$ and $Sr^{2+}$ co-doped ceria.

## 8.1 Mg and Sr Co-Doped Ceria

### 8.1.1 Introduction

Lanthanum gallate and doped ceria oxides have been proposed as solid electrolytes with high ionic conductivity in the intermediate temperature range (500-700 °C) [Fergus (2006); Kharton et al. (2004)]. Of these, ceria doped with aliovalent cations such as rare earth and alkaline earth ions has been widely investigated as solid electrolytes for IT-SOFCs [Inba et al. (1996); Steele (2000); Zha et al. (2003); Kharton et al. (2001); Wang et al. (2005)]. Substitution of aliovalent cations in ceria leads to generation of oxygen vacancies for charge compensation.

$$2\,CeO_2 \xrightarrow{M_2O_3} 2M'_{Ce} + 3O_O^{\times} + V_{\ddot{O}} \qquad (8.1)$$

$$CeO_2 \xrightarrow{MO} M''_{Ce} + 2O_O^{\times} + V_{\ddot{O}} \qquad (8.2)$$

where, the symbols are used in accordance with Kroger Vink notation of defects. Rare earth oxides have high solubility in ceria [Kharton et al. (2001)]. However, at high temperatures and low oxygen partial pressures, the electronic conductivity of doped ceria is considerably high. This is a problem for use of these materials as solid electrolyte for SOFCs. Co-doped ceria appears to be a potential solution for this problem [Wang et al. (2005)]. Gadolinium (Gd) and samarium (Sm) doped ceria have been widely used [Tianshu et al. (2002); Abrantes et al. (2003)] because these have lattice parameter almost equal to ceria. Their substitution produces very small strain in the lattice. This reduces the activation energy for diffusion of oxide ions [Kim (1989)]. This has also been confirmed by atomistic computer simulation studies based on the binding energy between the trivalent cations and oxygen vacancies and the corresponding lattice relaxation energy [Minervini et al. (1999)]. But Gd and Sm are very costly.

Alkaline earth oxides, such as CaO [Arai et al. (1986); Garnier et al. (1976)], SrO [Yahiro et al. (1986); Blumenthal et al. (1976)] and MgO have been used as dopant in $CeO_2$ to reduce the cost. Cho et al. (2007) studied the scavenging effect of SrO. It reacts with $SiO_2$ and the resulting silicate material segregates at triple point junction of the grain boundaries. This reduces the grain boundaries resistance. However, only a few reports on MgO doped ceria exist in the literature. Limited solubility of MgO in ceria has been reported due to difference in ionic radius of $Ce^{4+}$ (0.97Å) and $Mg^{2+}$ (0.89 Å) [Yahiro et al. (1988)] as well as their valency. $Ce_{0.90}Mg_{0.10}O_{1.90}$ exhibits very low conductivity ($2\times10^{-3}$ S-cm$^{-1}$) at 700 $^{o}$C [Wang et al. (2004)]. Solubility of SrO in ceria is between 5 and 10 mol% for the same reason (ionic radius of $Sr^{2+}$ is 1.26 Å) [Yahiro et al. (1988)]. It was considered worthwhile to investigate the conductivity of ceria co-doped with one smaller cation ($Mg^{2+}$) and one larger cation ($Sr^{2+}$) as compared to $Ce^{4+}$ so that the elastic strain generated is small. This is expected to enhance the ionic conductivity as well as reduce the cost of the electrolyte.

Hence, the primary objective of the present work is to develop new cost effective ceria based solid electrolytes having high ionic conductivity in the IT-range. Therefore a few compositions in the system $Ce_{0.90}Mg_{0.10-x}Sr_xO_{1.90}$ [(x = 0.00, CMO10), (0.02, CM8S2), (0.04, CM6S4) and (0.06, CM4S6)] keeping the total number of oxygen vacancies same, have been prepared and characterized. Scavenging effect of Sr in Mg-doped ceria may have an advantageous effect on the overall conductivity because it can hinder the formation of a continuous and uniform siliceous phase along the grain boundaries.

### 8.1.2 Results and discussion

### (a) Crystal structure and phases

To confirm the complete dissolution of the dopants in $CeO_2$, XRD patterns of all the calcined and sintered samples are recorded. Diffraction patterns are indexed on the basis of fluorite structure similar to $CeO_2$ using JCPDS file no. 43-1002. XRD patterns of the calcined samples are the same as that of the sintered samples except that the peaks become sharp after sintering. This is due to the grain growth during sintering. Diffraction peaks of the calcined samples are broad. Average crystallite size of the calcined powders has been found to be in the range 10-26 nm using Scherrer's formula for X-ray line broadening (Table. 8.1). Fig. 8.1 shows XRD patterns of the sintered samples. All the samples are single phase having cubic fluorite structure similar to $CeO_2$.

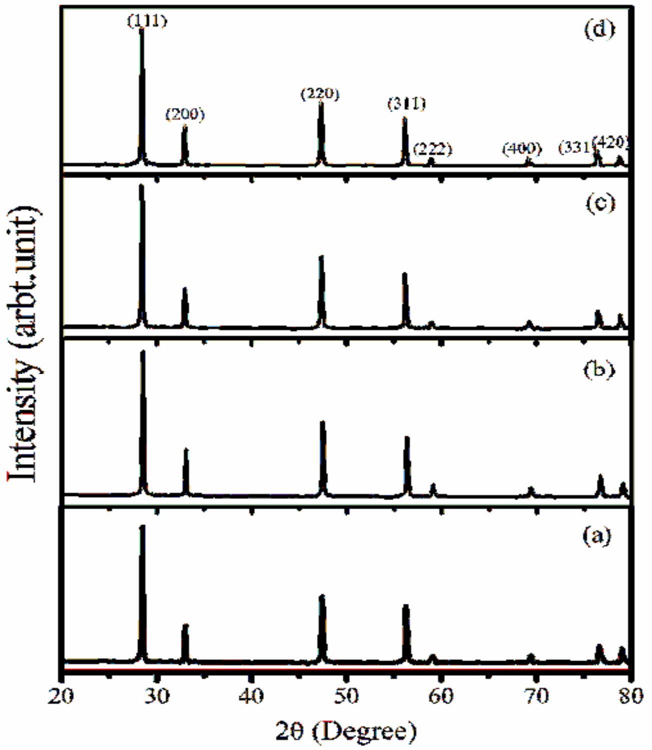

**Fig. 8.1 X-ray diffraction patterns of the sintered samples of compositions (a) CMO10 (b) CM8S2 (c) CM6S4 and (d) CM4S6 in the system $Ce_{0.90}Mg_{0.10-x}Sr_xO_{1.90}$**

It is observed that 2θ values of co-doped ceria shift slightly toward lower angles with increasing Sr content. The ionic radius increases in the order $Mg^{2+} < Ce^{4+} < Sr^{2+}$. Therefore substitution of $Sr^{2+}$ in $CeO_2$ in place of $Mg^{2+}$ increases the lattice parameter (Table. 8.1). Samples sintered at 1350 $^{o}$C for 4 hrs have densities more than 96% of the theoretical values (Table 8.1).

**Table. 8.1 Crystallite size, lattice parameter and % theoretical density of various compositions in the system $Ce_{0.90}Mg_{0.10-x}Sr_xO_{1.90}$**

| S. No. | x | Sample code | Crystallite size (nm) | Lattice parameter (Å) | % TD |
|---|---|---|---|---|---|
| 1. | 0.0 | CMO10 | 10 | 5.4099+/-0.0002 | 97.5 |
| 2. | 0.02 | CM8S2 | 11 | 5.4134+/-0.0026 | 97.5 |
| 3. | 0.04 | CM6S4 | 22 | 5.4260+/-0.0006 | 96.0 |
| 4. | 0.06 | CM4S6 | 26 | 5.4299+/-0.0005 | 97.0 |

### (b) Microstructure

Fig. 8.2 shows SEM micrographs of the fractured surfaces of the sintered samples. Micrographs show well-defined grains separated by the grain boundaries. As strontium content increases, a narrowing of grain size distribution is observed. Average grain size of the compositions, CMO10, CM8S2, CM6S4 and CM4S6 determined by linear intercept method as well as using ImageJ software is approx. 3.6, 2.1, 1.0, and 2.0 µm respectively. It is observed from Fig. 8.2 that the average grain size decreases with increasing concentration of Sr up to x = 0.04 indicating that Sr acts as a grain growth inhibitor. This may be due to segregation of $Sr^{2+}$ at the grain boundaries due to elastic strain arising out of size mismatch between $Sr^{2+}$ and $Ce^{4+}$. The grain boundaries are regions of high energy because of disorder. Therefore, the dopant ions can be accommodated in the grain boundaries with the minimum expenditure of extra energy i.e. dopants tends to segregate to the grain boundaries. The reason for increasing the grain size for the sample CM4S6 is not clear at present.

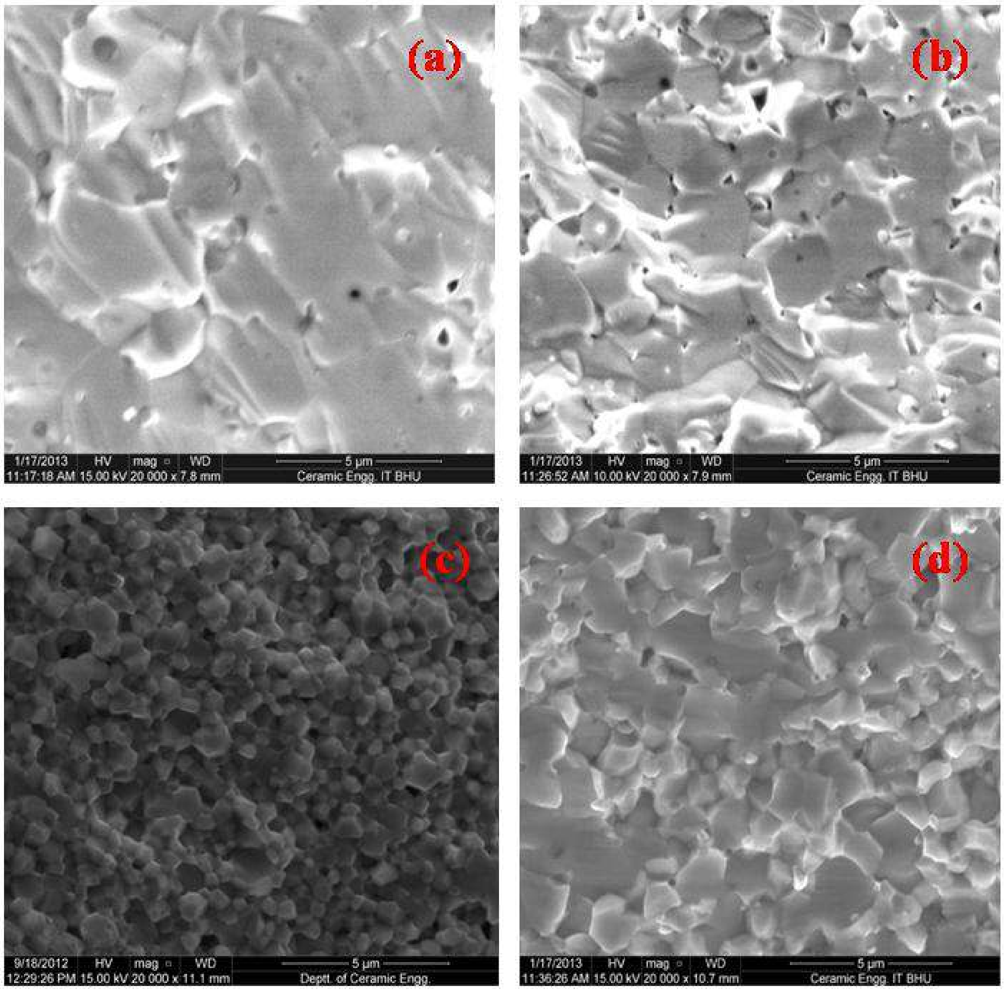

**Fig. 8.2 SEM micrographs of the fractured surfaces of the sintered samples in the system $Ce_{0.90}Mg_{0.10-x}Sr_xO_{1.90}$ for (a) CMO10 (b) CM8S2 (c) CM6S4 and (d) CM4S6**

Fig. 8.3 shows the EDS spectra of the composition CMO10 at two different points. Spectrum 1 is from a point in the grain and spectrum 2 is from a point at the grain boundary. Both the spectra are the same except that Si is present at the grain boundary. EDS spectra of the composition, CM6S4 at three points in the grain, at the grain boundary and at triple point is shown in Fig. 8.4.

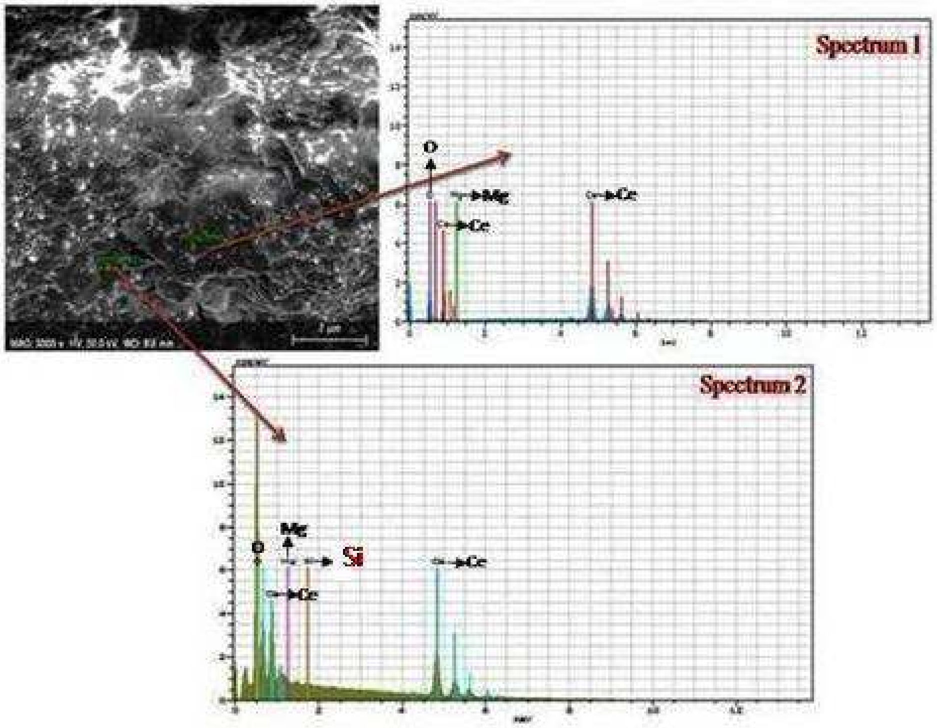

**Fig. 8.3 EDX spectrum of the composition CMO10 at two different points: Spectrum 1(in the grain) Spectrum 2 (at the grain boundary)**

It is seen that all the spectra at three points are the same except that Si is present at triple point. But Si is not present at the grain boundary. This is due to scavenging of siliceous impurity by $Sr^{2+}$. Sr reacts with Si to form some silicate phases which segregate at triple point rather at the boundaries. This leaves clean grain boundaries for grain to grain contacts. This results in fast diffusion of oxide ions across the grain boundaries. The exact composition and morphology of the silicate phases needs to be confirmed by STEM equipped with EELS and EDXM [Gerhardt et al. (1986)].

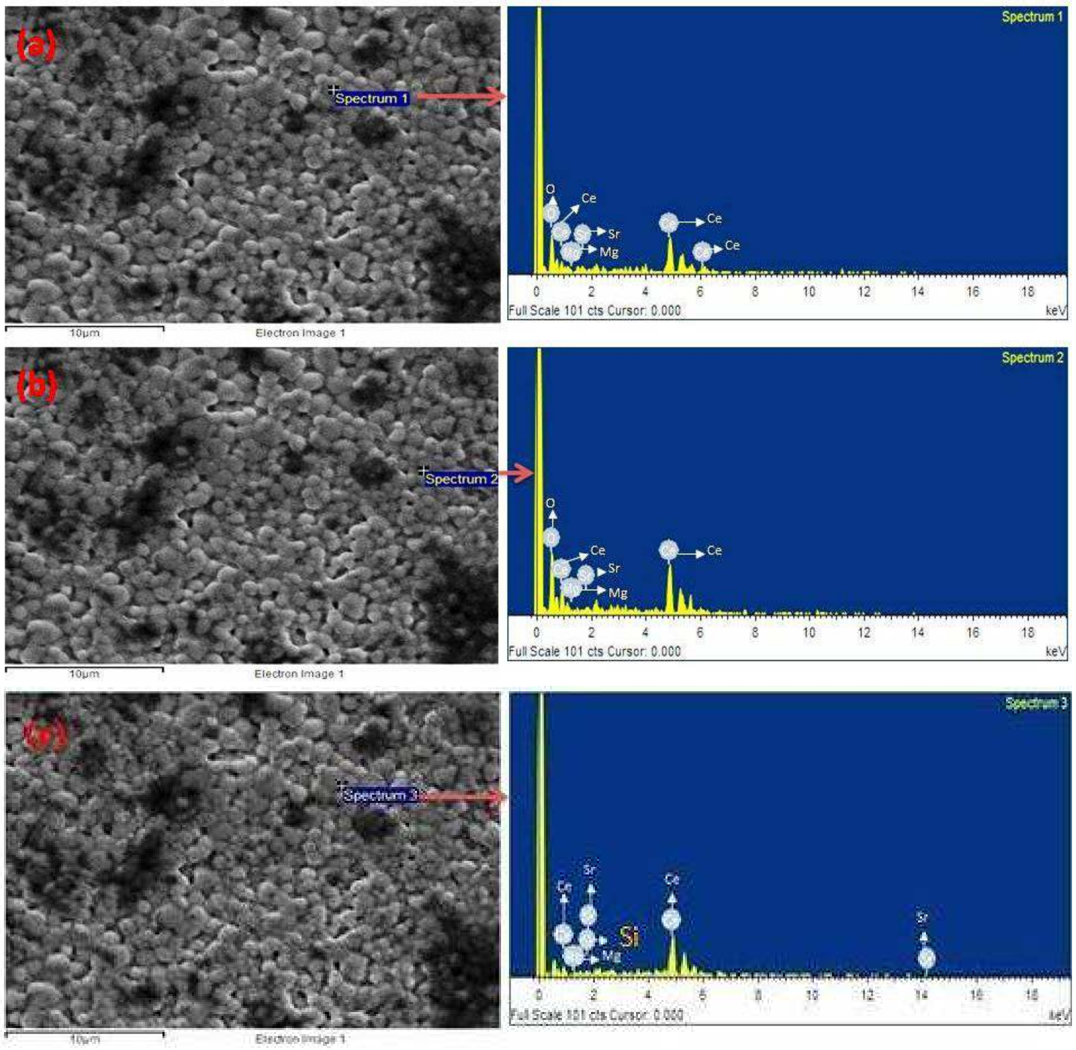

**Fig. 8.4 EDS spectrum of the composition CM6S4 at three different points: (a) in the grain, (b) at the grain boundary and (c) at triple point**

### (c) Electrical conductivity

Complex plane impedance plots of all the compositions are shown in Figs. 8.5-8.8. For the composition, CMO10, only one arc associated with a spike has been observed in the temperature range 200-400 °C. The arc passing from the origin in the high frequency region is ascribed to contribution of the grains and the spike in the intermediate frequency range corresponds to contribution of the grain boundaries to the total resistance. Relaxation frequency of the polarization processes increases with increasing temperature. Therefore, the arc due to the grains disappears above 400 °C and the grain boundaries arc is clearly seen above this temperature. At higher temperatures, only the arc due to grain boundaries has been observed. In the case of the composition, CM8S2, two arcs ascribed to the contribution of the grains and the grain boundaries have been observed at 200 and 225 °C. Beyond 250 °C, electrode arc starts appearing. The arc due to the grains disappears above 400 °C. The data are plotted in the insets to clearly see the contribution of the grain boundaries. One intermediate and one low frequency arcs have been observed at temperatures >400 °C. The grains and grain boundaries arcs have the capacitances in the pF ($10^{-10}$-$10^{-12}$) and nF ($10^{-7}$-$10^{-9}$) range respectively [Hodge et al. (1976)]. The capacitance is determined from the relation $2\pi f_{max}RC = 1$, where $f_{\max}$ is the frequency at the highest point of the arc, R is the resistance and C is the capacitance.

The impedance plots are fitted to an equivalent circuit to obtain the contribution of the grains and the grain boundaries. In the case of composition, CMO10, only the contribution of the grains is seen clearly in the temperature range 200-400 °C. Therefore, only the arc of grains is fitted to an equivalent circuit containing one ($R_1$-CPE1) element connected in parallel. Above 400 °C, the arc of the grains shift towards higher frequency and the contribution of the grain boundaries is clearly seen. Therefore, the impedance plots are fitted using $R_1$-($R_2$-CPE1) circuit above 400 °C.

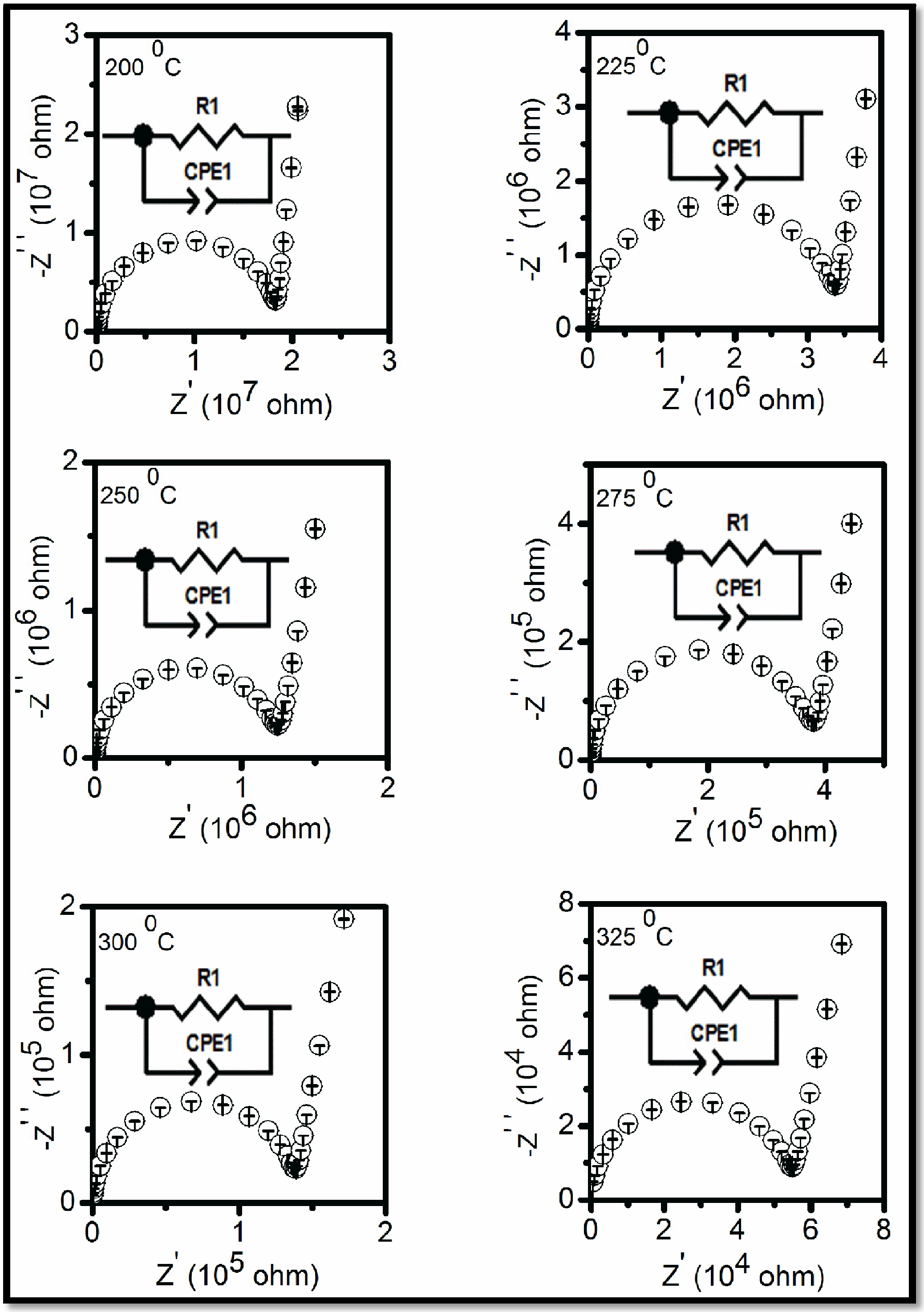

**Fig. 8.5 Complex plane impedance plots of the composition CMO10 at different temperatures**

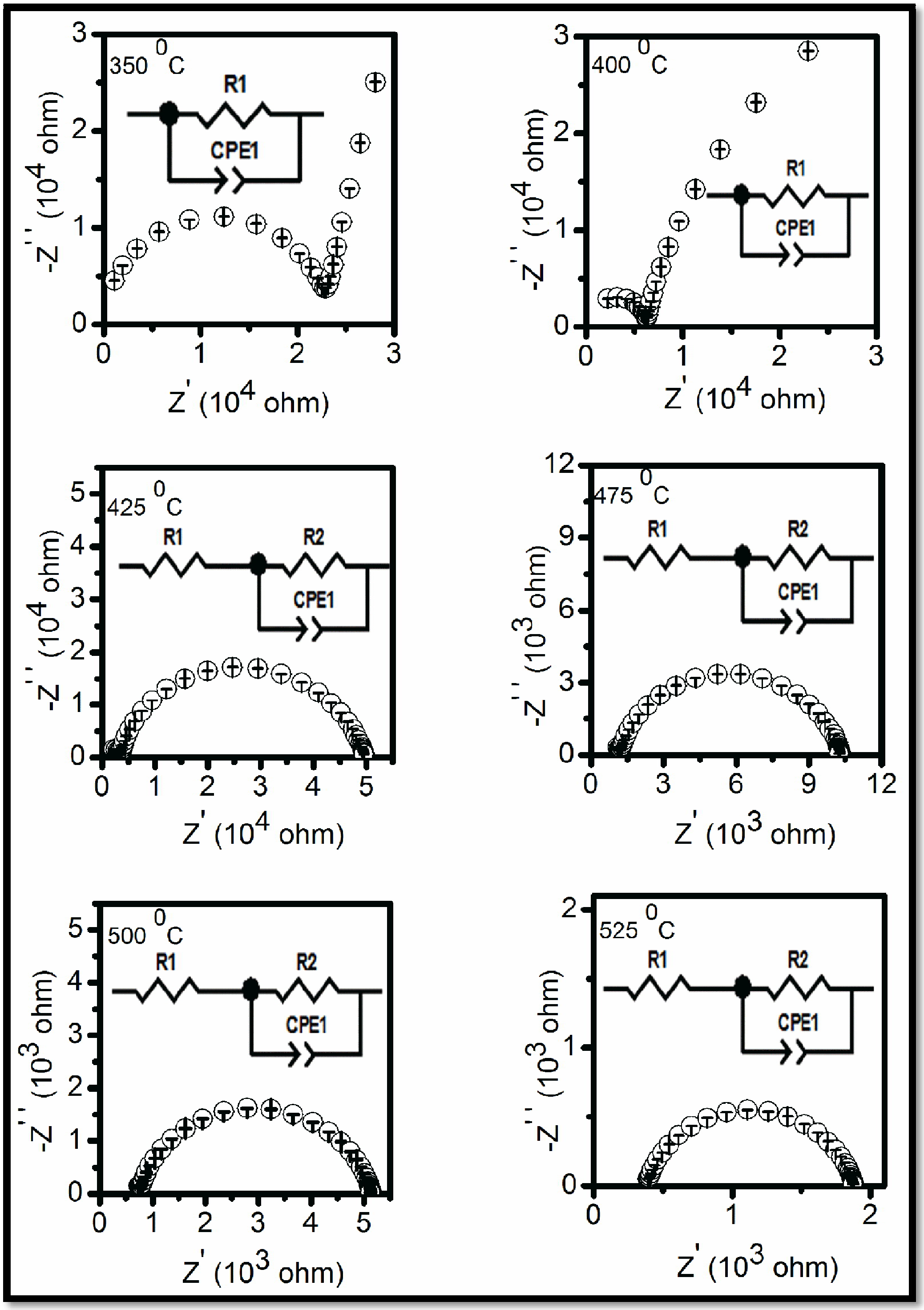

**Fig. 8.5 Complex plane impedance plots of the composition CMO10 at different temperatures**

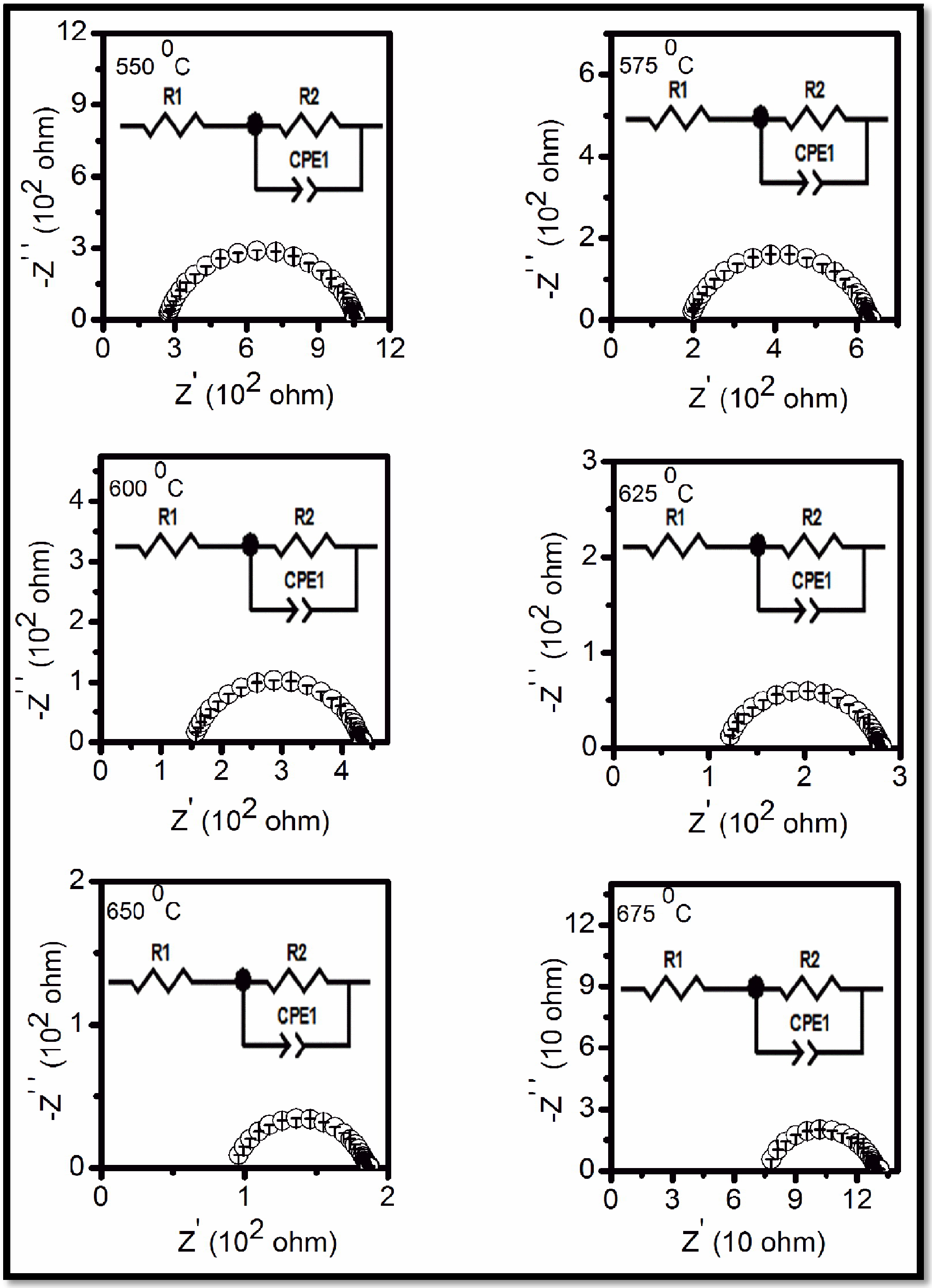

Fig. 8.5 Complex plane impedance plots of the composition CMO10 at different temperatures.

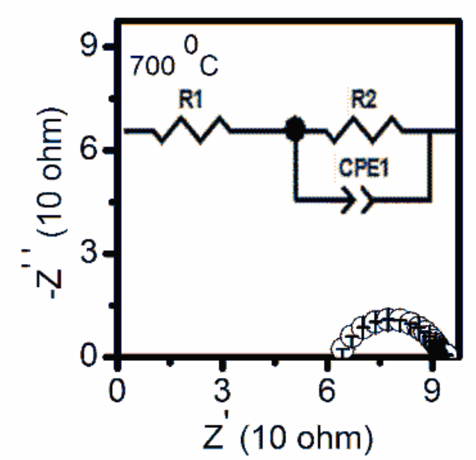

**Fig. 8.5 Complex plane impedance plots of the composition CMO10 at 700** °C

For the compositions, CM6S4 and CM4S6, three arcs are seen in the temperature range 200-275 °C. The high and intermediate frequency arcs are ascribed to contribution of the grains and the grain boundaries and a low frequency tail is attributed to the electrode/electrolyte interface polarization. The data is plotted in the insets to clearly see the contribution of the grain boundaries. The arcs due to the grains and the grain boundaries disappear above 275 and 475 °C respectively. Beyond 500 °C, only electrode contribution is seen.

In the present investigation, only the arcs of the grains and the grain boundaries are fitted. The electrode arc is not fitted because the sum of the resistance of the grains and the grain boundaries are equal to the total resistance of the sample. The intercept on the real axis at the higher frequency side of the electrode arc has been taken as total resistance of the sample when both the grains and grain boundaries arcs disappear.

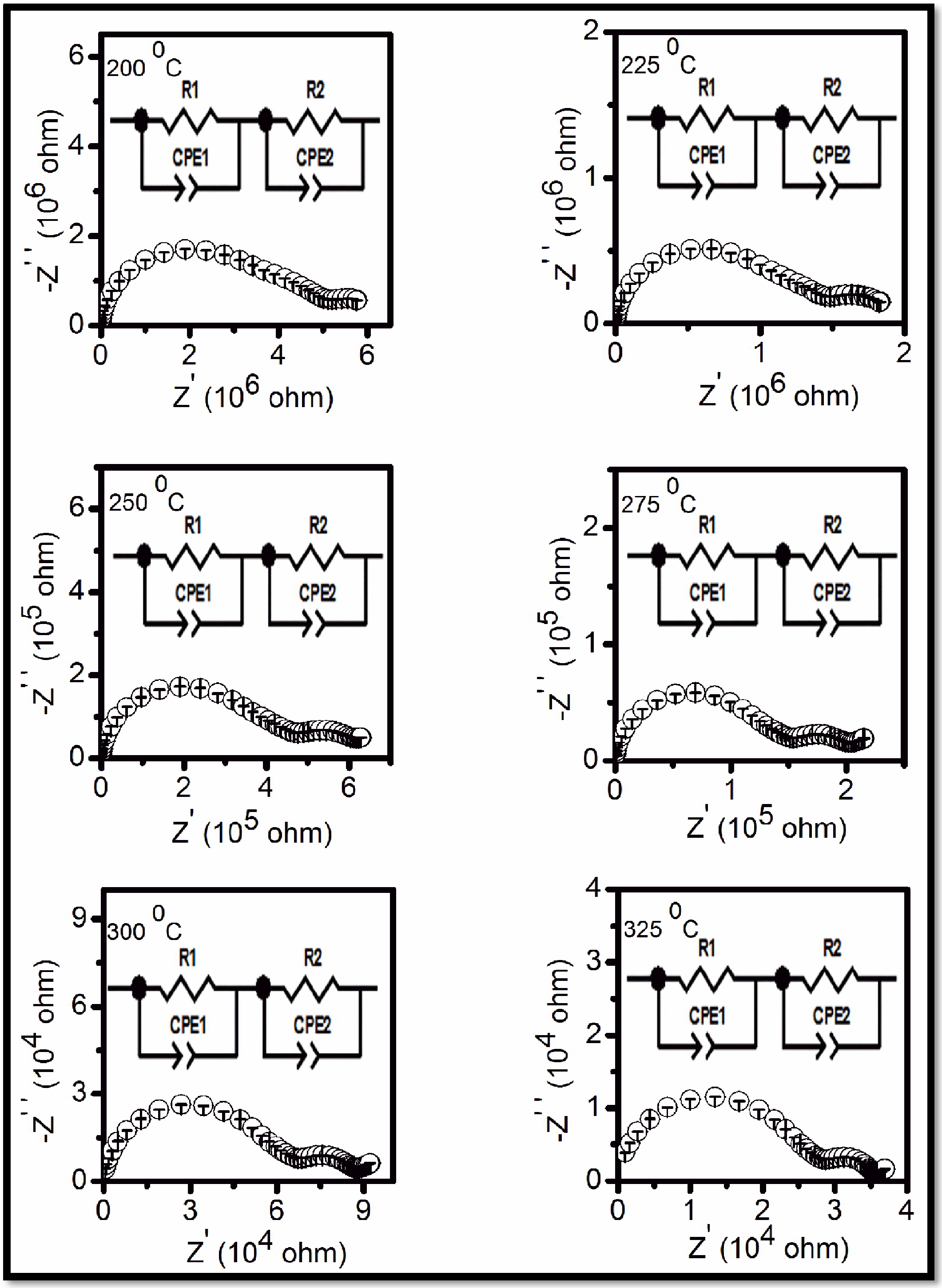

**Fig. 8.6 Complex plane impedance plots of the composition CM8S2 at different temperatures**

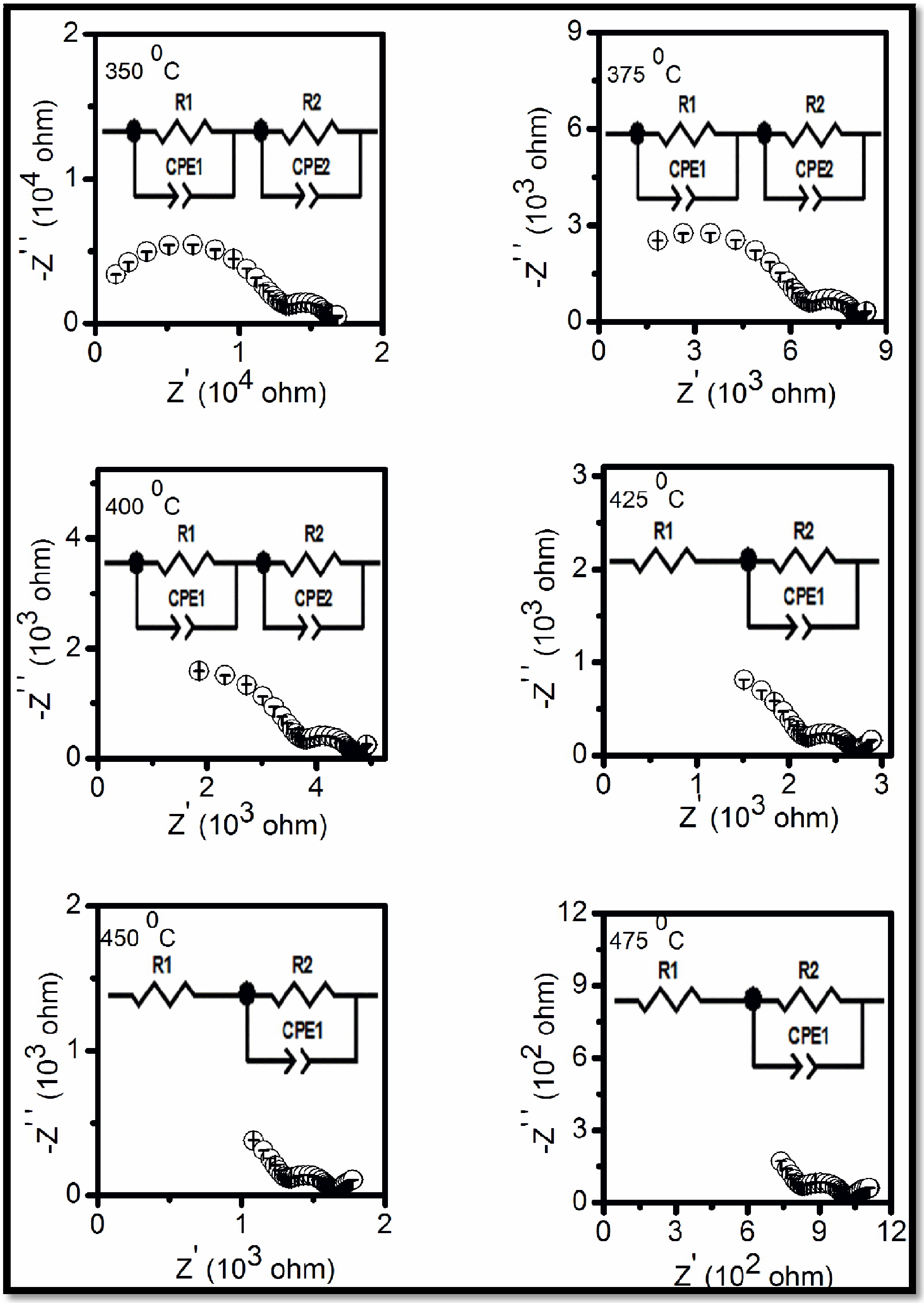

Fig. 8.6 Complex plane impedance plots of the composition CM8S2 at different temperatures

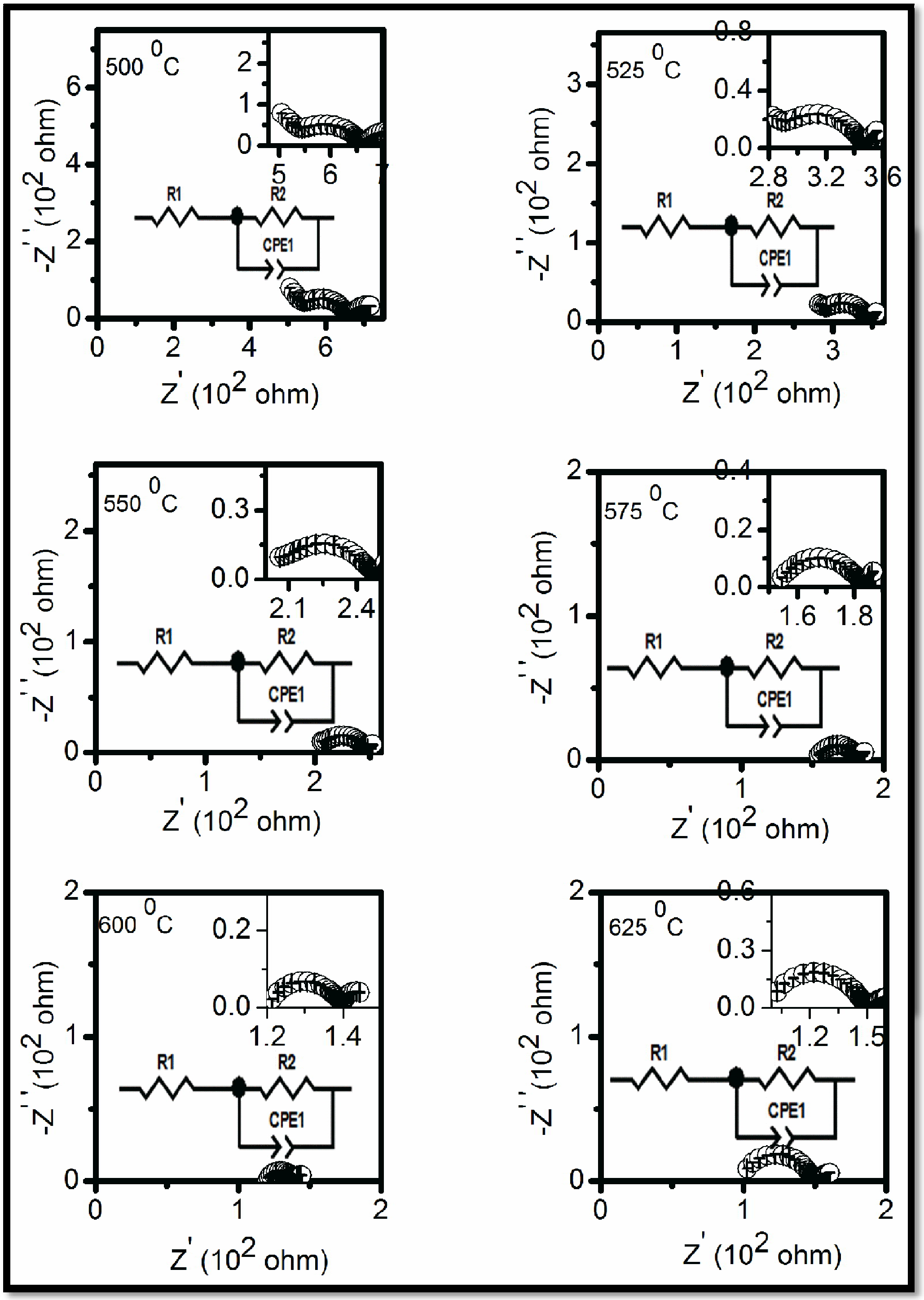

**Fig. 8.6 Complex plane impedance plots of the composition CM8S2 at different temperatures.**

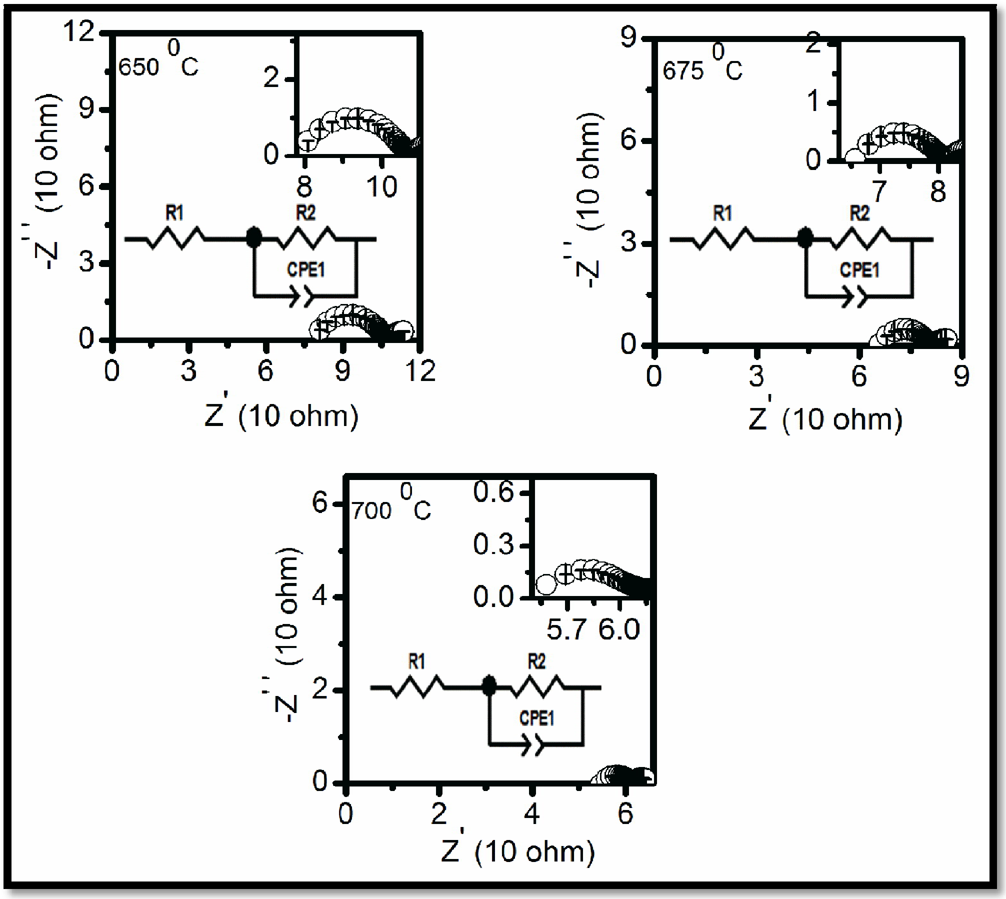

**Fig. 8.6 Complex plane impedance plots of the composition CM8S2 at different temperatures**

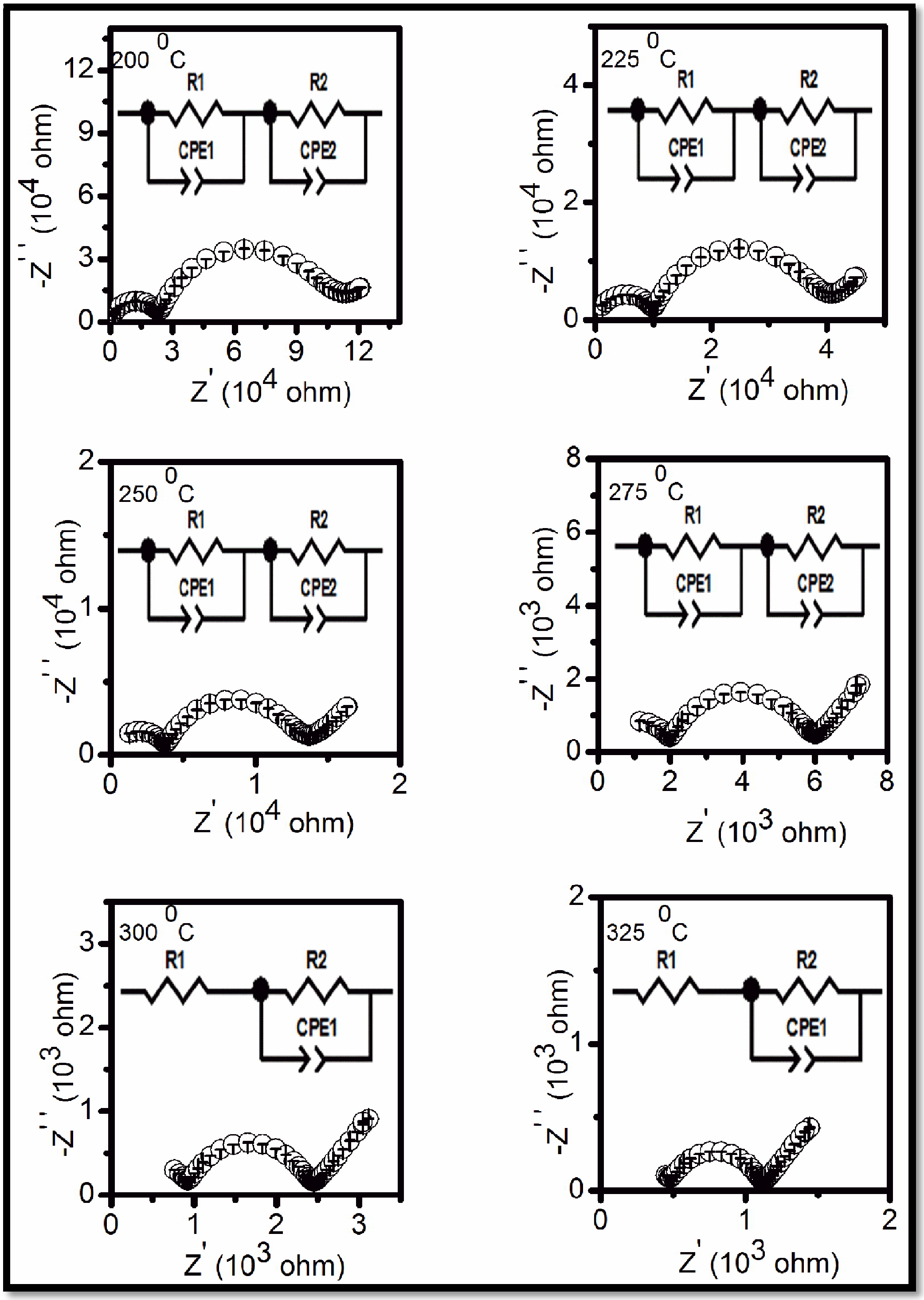

**Fig. 8.7 Complex plane impedance plots of the composition CM6S4 at different temperatures**

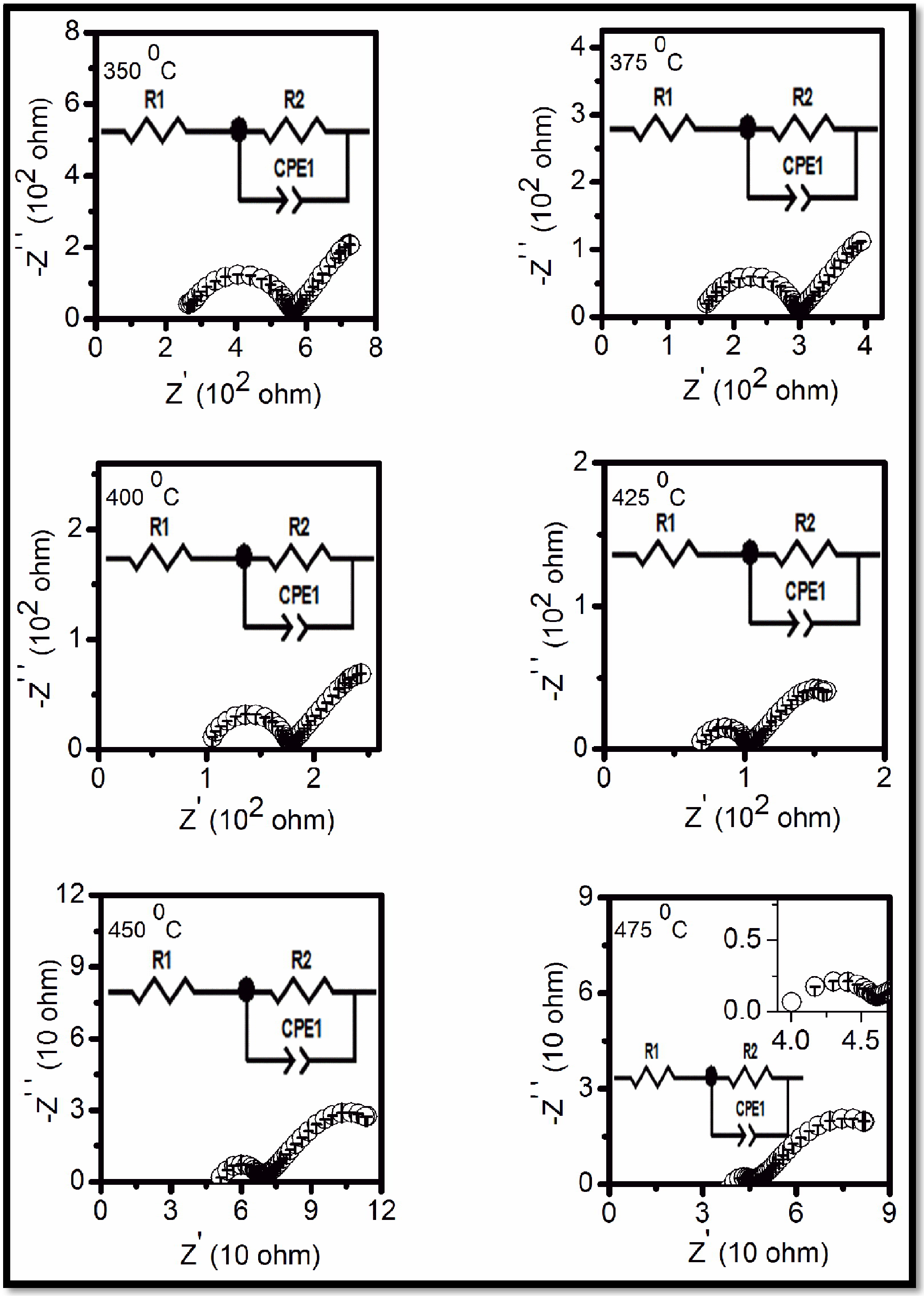

Fig. 8.7 Complex plane impedance plots of the composition CM6S4 at different temperatures

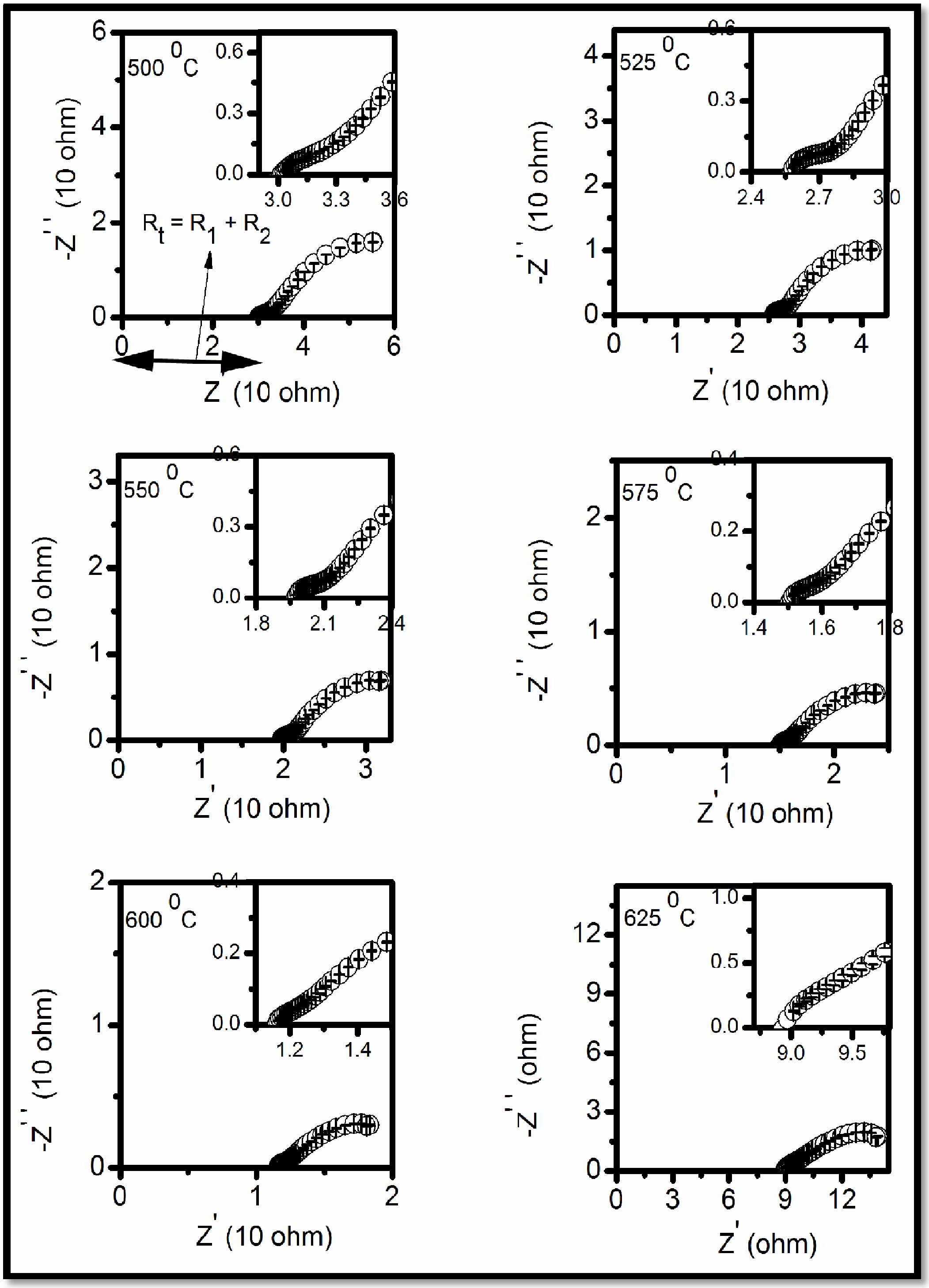

Fig. 8.7 Complex plane impedance plots of the composition CM6S4 at different temperatures

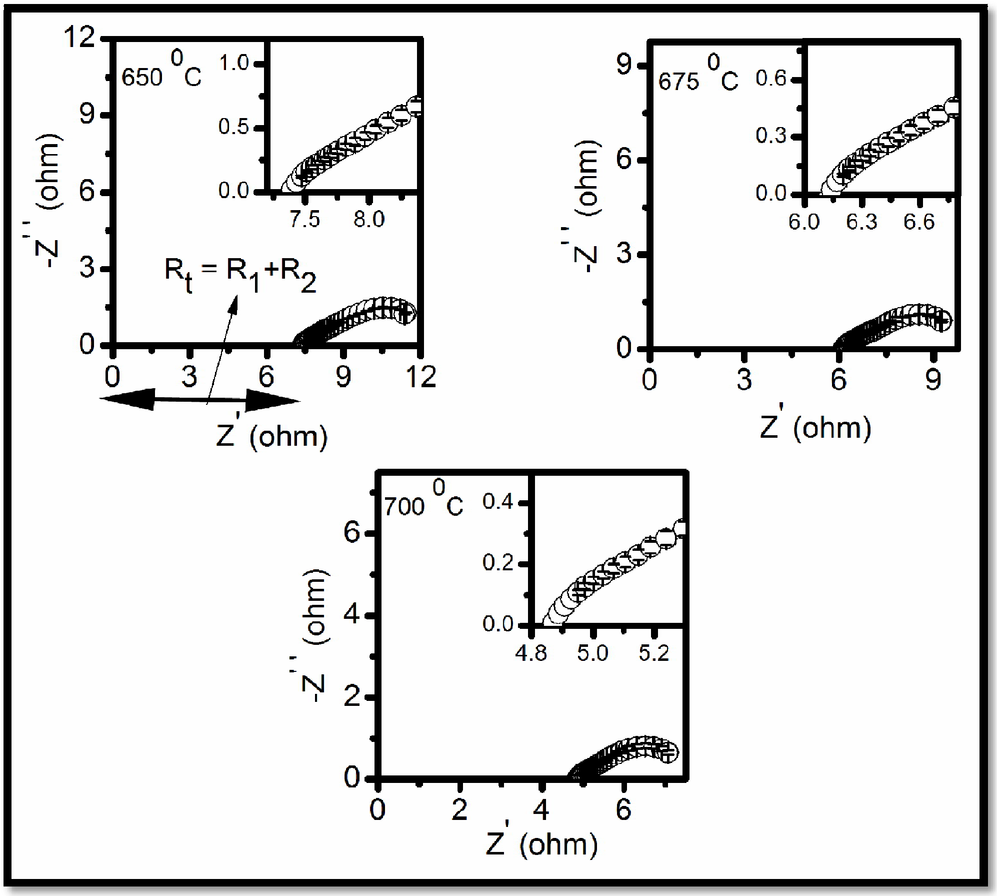

**Fig. 8.7 Complex plane impedance plots of the composition CM6S4 at different temperatures**

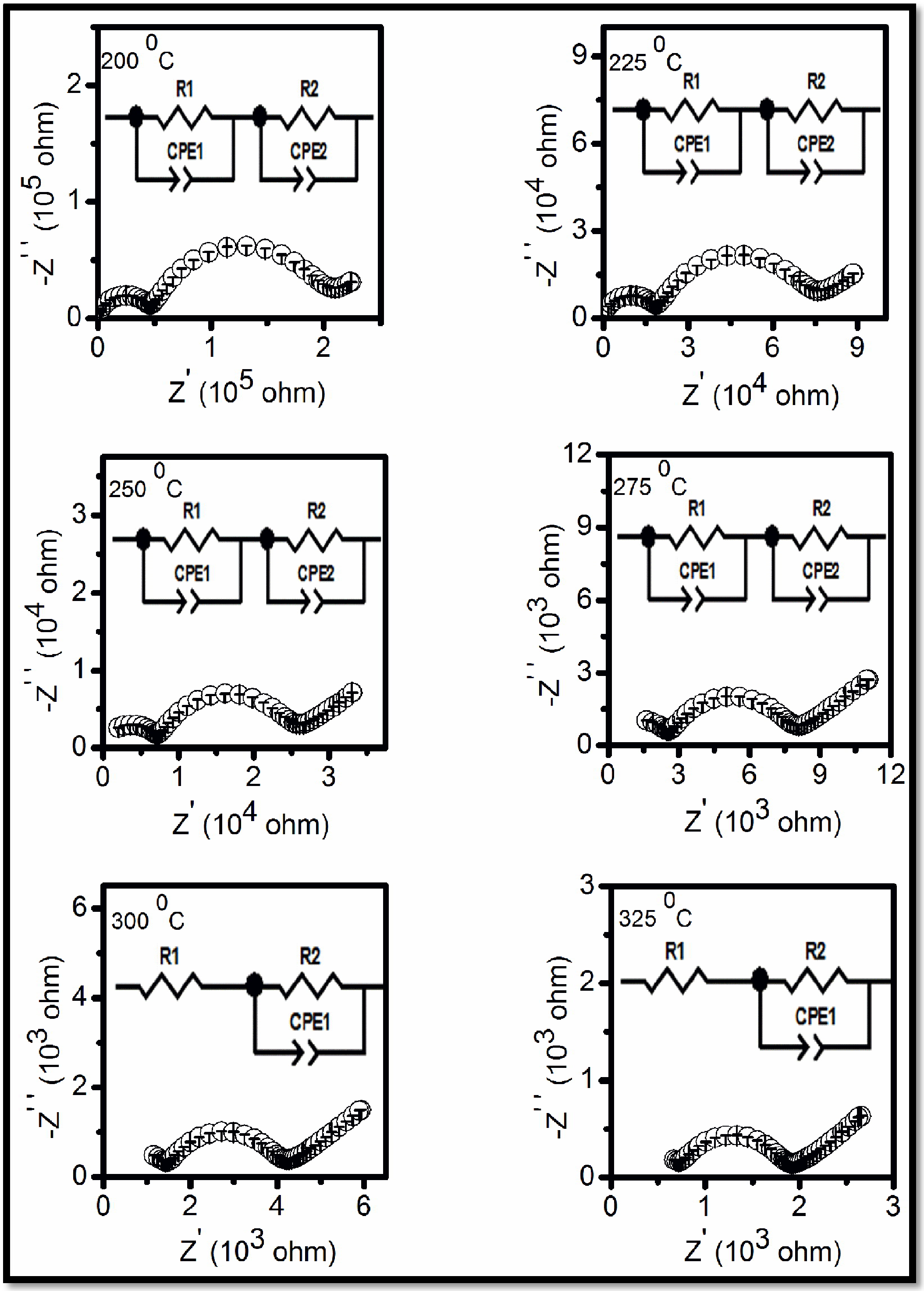

**Fig. 8.8 Complex plane impedance plots of the composition CM4S6 at different temperatures**

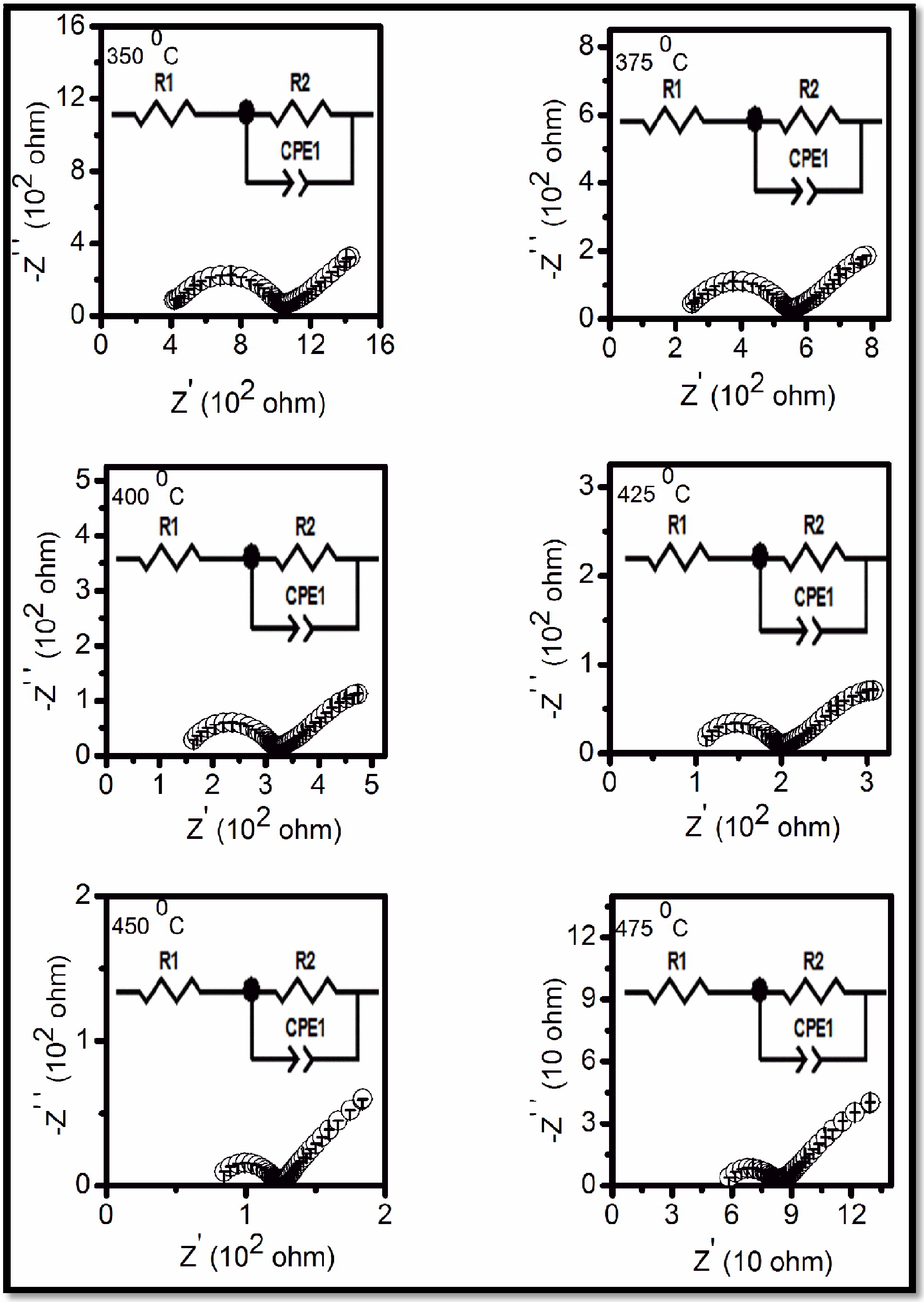

**Fig. 8.8 Complex plane impedance plots of the composition CM4S6 at different temperatures**

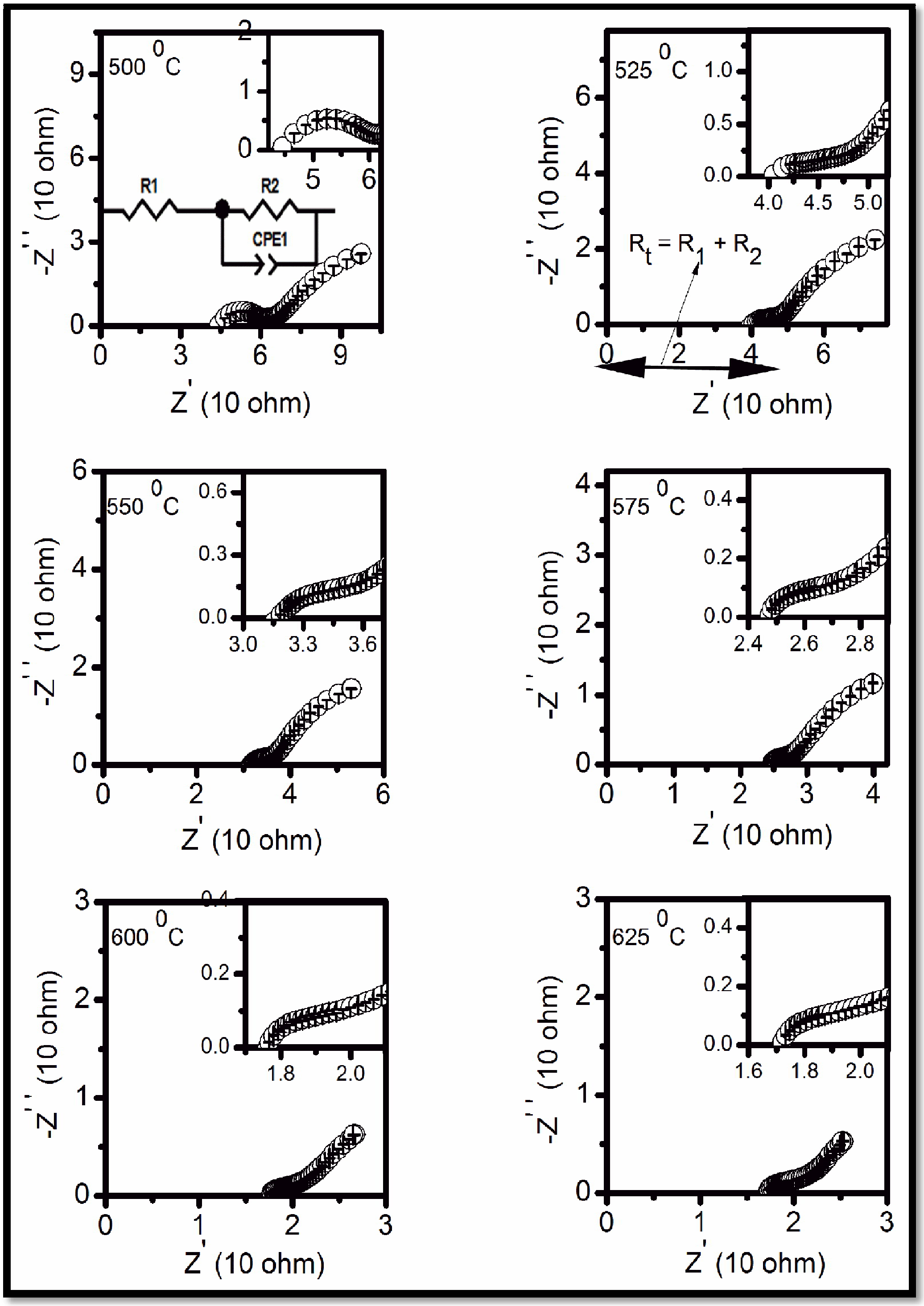

**Fig. 8.8 Complex plane impedance plots of the composition CM4S6 at different temperatures**

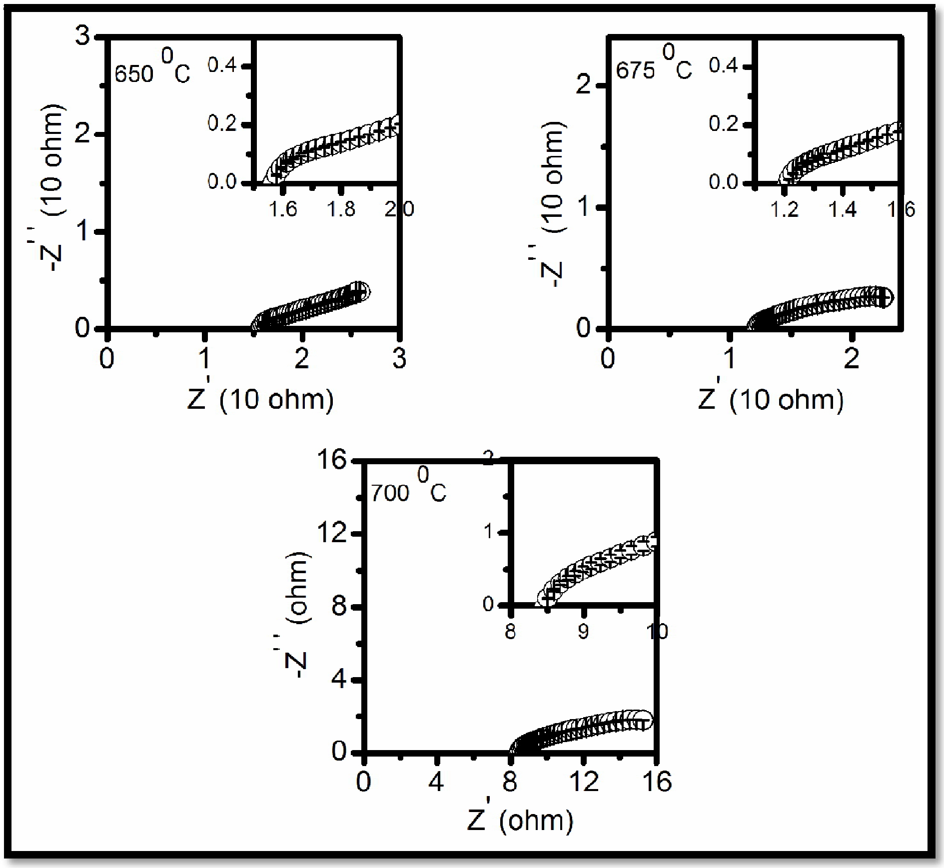

**Fig. 8.8 Complex plane impedance plots of the composition CM4S6 at different temperatures**

Fig. 8.9 shows the Arrhenius plots for the grains (bulk), grain boundaries and the total ionic conductivity of all the samples. It is seen from Fig. 8.9 that the bulk conductivity first increases with increasing strontium content up to 4 mol% (x = 0.04) and then decreases above this concentration. The enhancement in the bulk conductivity may be ascribed to the suppression of the ordering of oxygen vacancies and increase in the configurational entropy (S). This leads to an increase in the bulk conductivity due to decrease in the activation energy for diffusion of $O^{2-}$ ions [Yamamura et al. (2000)].Values of S for all the compositions are given in Table. 8.3. It is noted from this table that S increases up to x = 0.04 and thereafter it becomes constant. As the concentration of Sr increases, strain in the lattice increases due to larger size of $Sr^{2+}$ (1.26 Å) compared to $Mg^{2+}$ (0.89 Å).

This causes an increase in the number of associated defect pairs $[Sr_{Ce}'' - V_O^{\bullet\bullet}]^{\times}$ leading to increase in the association enthalpy. This causes a decrease in the conductivity.

It is also noted from Fig. 8.9 that Arrhenius plots of the bulk conductivity show a change in the slope at 400 $^{o}$C which is interpreted as a transition from the associated defect pairs $[Sr_{Ce}'' - V_O^{\bullet\bullet}]^{\times}$ to dissociated defects (free oxygen vacancies). At low temperatures, concentration of charge carriers is determined by the thermodynamic equilibrium between the free defects and the associated defect pairs viz. $[Mg_{Ce}'' - V_O^{\bullet\bullet}]^{\times}$ and $[Sr_{Ce}'' - V_O^{\bullet\bullet}]^{\times}$. In the low temperature range, the activation energy is the sum of migration enthalpy and defect association enthalpy and in the high temperature region it contains only the migration enthalpy. Activation energy of conduction for the grains, $E_g$ is determined by fitting the data in Fig. 8.9 to Arrhenius equation:

$$\sigma_g = \frac{\sigma_{0g}}{T} exp\left(\frac{-E_g}{kT}\right) \tag{8.3}$$

where, $\sigma_{0g}$ is the pre exponential factor, k is Boltzmann constant and T is absolute temperature. Values of $E_g$, measured at low and high temperature range are given in Table. 8.2.

The conductivity of the grain boundaries continuously increases with increasing strontium content up to 4 mol% as shown in Fig. 8.9. This may be due to scavenging effect of strontium to remove siliceous impurities present at the grain boundaries. To confirm the scavenging effect of strontium for grain boundaries, the influence of the grain boundaries conductivity on the total conductivity is evaluated through the blocking factor, $\alpha_R$. The lowest blocking factor, 0.42 has been observed in the composition CM6S4 while it is 0.95 for the composition CMO10. Therefore it is concluded that strontium is an effective grain boundary scavenger. Sr reacts with the Si present at the grain boundaries to form some silicate phases which segregate at the triple point of the grain boundaries. This leaves clean grain boundaries for grain to grain contacts.

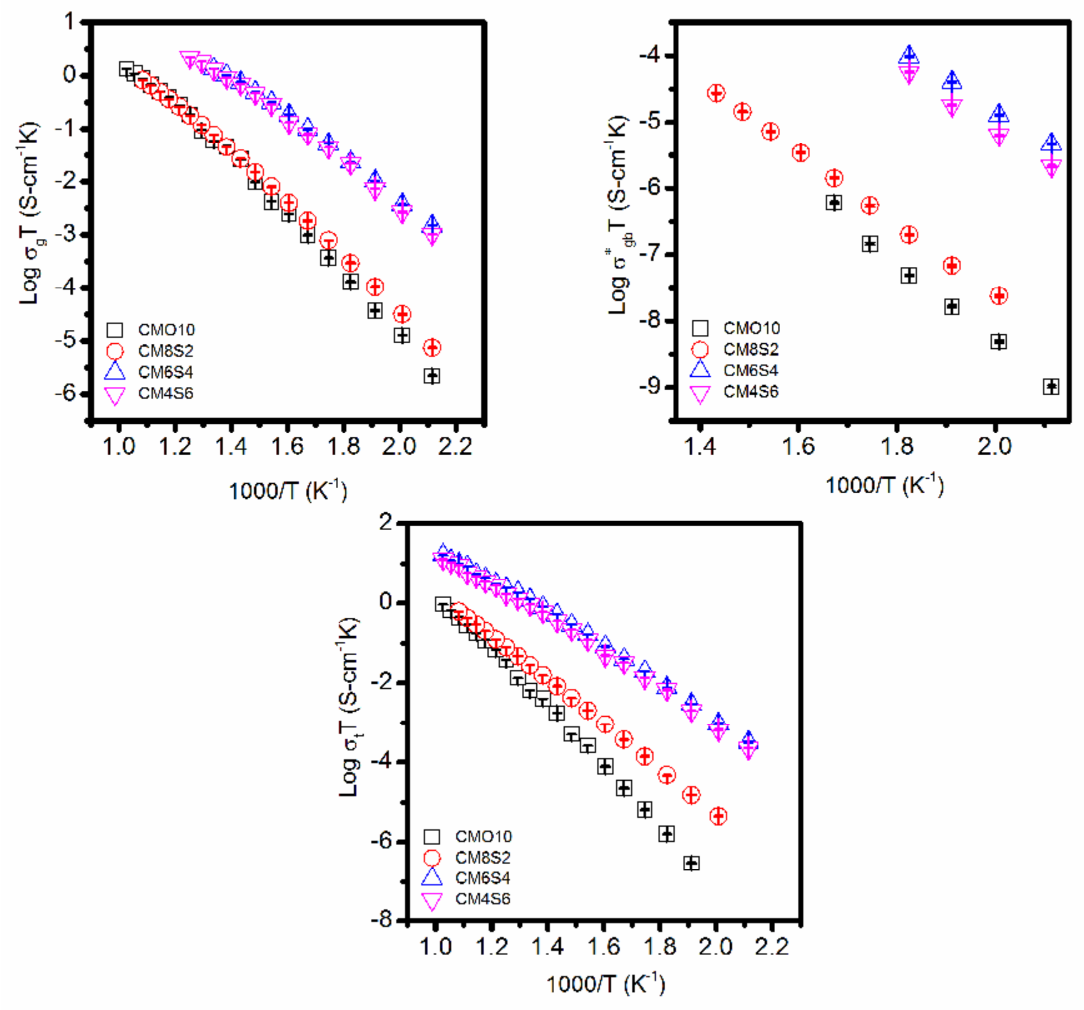

**Fig. 8.9 Arrhenius plots of the grains, grain boundaries and total conductivity in the system $Ce_{0.90}Mg_{0.10-x}Sr_xO_{1.90}$**

The exact composition, morphology and distribution of these phases needs to be confirmed using scanning transmission electron microscope (STEM) combined with energy dispersive X-ray microanalysis (EDXM) and electron energy loss spectroscopy (EELS) [Gerhardt et al. (1986)]. This is also in confirmation with the EDS of compositions CMO10 and CM6S4 i.e. Si is present only at the grain boundary of CMO10 while in case of CM6S4, Si is present at the triple point only. It is also observed from Fig. 8.9 that grain boundaries conductivity also depends on the average grain size. Small grain size samples exhibits higher grain boundaries conductivity because the area of the grain boundaries is so large that the finite amount of impurity contained in these samples is not sufficient to form a continuous and uniform glassy phase layer along the grain boundaries. This leaves the remaining grain boundaries area with clean grain to grain contact. Therefore, the transport of $O^{2-}$ ions across the clean boundaries is easy. This also influences the total conductivity observed in these samples. Activation energy of the conduction for the grain boundaries, $E_{gb}$ for all the compositions is determined by fitting the data in Fig. 8.9 to Arrhenius equation and is given in Table. 8.2. Value of $E_{gb}$ is less for the Sr co-doped samples and it is minimum for the sample, CM6S4. Fig. 8.9 shows that the total conductivity increases with increase in Sr concentration up to x = 0.04 and decreases for higher value of x. Activation energy for total ionic conductivity is given in Table. 8.2 and it is found to be minimum for the composition CM6S4.

**Table. 8.2 Activation energy for the conduction of grains ($E_g$) , grain boundaries ($E_{gb}$) and total ($E_t$) of various compositions in the system $Ce_{0.90}Mg_{0.10-x}Sr_xO_{1.90}$**

| S. No. | x | Sample code | $E_g$ (eV) | | $E_{gb}$ (eV) | $E_t$ (eV) |
|---|---|---|---|---|---|---|
| | | | 200-400 °C | 400-700 °C | | |
| 1. | 0.0 | CMO10 | 1.12 | 0.76 | 1.20 | 1.46 |
| 2. | 0.02 | CM8S2 | 1.02 | 0.79 | 1.07 | 1.11 |
| 3. | 0.04 | CM6S4 | 0.82 | 0.58 | 0.88 | 0.85 |
| 4. | 0.06 | CM4S6 | 0.84 | 0.59 | 0.97 | 0.87 |

Values of the total conductivity at 500 and 700 °C for all the compositions are given in Table. 8.3. Composition CM6S4 has the highest ionic conductivity among all the samples. Its conductivity is about 94 % higher than that of singly magnesium doped ceria. It is found that conductivity of the composition CM6S4 ($2.39\times10^{-3}$ S/cm) is higher than the values reported for the composition $Ce_{0.85}Ca_{0.09}Mg_{0.06}O_{1.85}$ under the same experimental conditions ($2.09\times10^{-3}$ S/cm) [Parkash et al. (2012)] at 500 °C. The maximum value of total ionic conductivity corresponds to the minimum activation energy in agreement with the Meyer-Neldel compensation rule [Meyer et al. (1937]. Partial substitution of Mg with Sr in $CeO_2$ has some opposite competiting effects. Ordering of oxygen vacancies is suppressed due to co-doping. This leads to decrease in the activation energy for migration of the $O^{2-}$ ions leading to increase in the conductivity. Secondly, on substitution of $Sr^{2+}$, binding energy of oxygen decreases as compared to that in $CeO_2$. This decreases the activation energy for the diffusion of oxygen ions leading to increase in the conductivity. SrO acts as a grain boundaries scavenger and decreases the resistivity of the grain boundaries as well as the total resistivity.

**Table. 8.3 Total conductivity at 500 and 700 °C and configurational entropy (S) of various compositions in the system $Ce_{0.90}Mg_{0.10-x}Sr_xO_{1.90}$**

| **S. No.** | **x** | **Sample code** | **$\sigma_t$ at 500 °C (S/cm)** | **$\sigma_t$ at 700 °C (S/cm)** | **S (J/mol-K)** |
|---|---|---|---|---|---|
| 1. | 0.0 | CMO10 | $1.71\times10^{-5}$ | $9.53\times10^{-4}$ | 2.70 |
| 2. | 0.02 | CM8S2 | $6.05\times10^{-5}$ | $1.42\times10^{-3}$ | 3.12 |
| 3. | 0.04 | CM6S4 | $2.40\times10^{-3}$ | $2.00\times10^{-2}$ | 3.26 |
| 4. | 0.06 | CM4S6 | $1.64\times10^{-3}$ | $1.25\times10^{-2}$ | 3.26 |

As the concentration of Sr increases, strain in the lattice increases due to larger size of $Sr^{2+}$ (1.26 Å) compared to $Mg^{2+}$ (0.89 Å). This causes an increase in the number of associated defect pairs $[Sr''_{Ce} - V_O^{\bullet\bullet}]^{\times}$ leading to increase in the association enthalpy. This leads to decrease in the ionic conductivity. First three factors seems to dominate up to x = 0.04 while the last one factor starts dominating for x > 0.04 leading to decrease in the conductivity. Since the composition, CM6S4 shows the highest conductivity among all the samples.

Use of this composition as a solid electrolyte for IT-SOFCs will reduce the cost because it contains only alkaline earth ions. Alkaline earth ions are cheaper than the rare earth ions.

### 8.1.3 Conclusion

- Nanocrystalline Mg and Sr co-doped samples in the system $Ce_{0.90}Mg_{0.10-x}Sr_xO_{1.90}$ have been synthesized successfully using citrate-nitrate gel auto-combustion route.
- All the samples in this system have fluorite structure similar to ceria.
- All the samples sintered at 1350 °C for 4 hrs have density >96% of the theoretical value.
- An enhancement in the conductivity of the system $Ce_{0.90}Mg_{0.10-x}Sr_xO_{1.90}$ indicates that a partial substitution of magnesium and strontium in ceria leads to increase in the conductivity as compared to ceria singly doped with Mg.
- Grain boundaries conductivity increases up to $x = 0.04$ due to scavenging effect of Sr and decrease in the average grain size of the samples.
- Composition, CM6S4 shows high ionic conductivity and low activation energy than that the ceria doped with magnesium only.
- Use of this material as a solid electrolyte for IT-SOFCs will reduce the cost as compared to earlier one in which one rare earth and one alkaline earth ions are present.

## 8.4 Nanocomposites of Mg and Sr Co-doped Ceria (CM6S4)

### 8.2.1 Introduction

Solid electrolyte having adequate high oxide ion conductivity in the intermediate temperature range (500-700 °C) is a key component of IT-SOFCs [Steele et al. (2001)]. Lower temperature of operation of these cells as compared to the currently used SOFCs based on yttria stabilized zirconia (YSZ) facilitates the use of cheaper materials for various components of the cells/cells stack. Some doped and co-doped ceria based solid electrolytes e.g. $Ce_{0.80}Sm_{0.20}O_{1.90}$ (SDC) [Omar et al. (2006)],

$Ce_{0.85}Gd_{0.15}O_{1.925}$ [Singh et al. (2011)], $Ce_{1-x-y}Mg_xLa_yO_{2-\delta}$ [Singh et al. (2012)], $Ce_{0.80}Gd_{0.20}O_{1.90}$ (GDC), [Sha et al. (2007)] and $Ce_{0.80}Gd_{0.2-x}Sm_xO_{1.9}$ [Tsung et al. (2007)] etc has been reported to possess ionic conductivity of ~$10^{-2}$ S/cm at 500-700 °C. One problem associated with the use of ceria based electrolytes in this temperature range is the tendency of $Ce^{4+}$ to get reduced to $Ce^{3+}$ in the reducing atmosphere at the anode. This gives rise to electronic conductivity leading to short circuiting of the cell. The research has, therefore, been focused to decrease the operating temperature of SOFCs below 600 °C abbreviated as low temperature SOFCs (LT-SOFCs) [Goodenough (2000); Li et al. (2007); Huang et al. (2008)].

Ceria/salt based composites especially ceria/carbonates show much higher ionic conductivity in the range 0.01-1 S/cm and a power density of 300-1100 $mW/cm^2$ at 400-600 °C [Huang et al. (2007)]. In the above reported results, it has been observed that the composition, $Ce_{0.90}Mg_{0.06}Sr_{0.04}O_{1.90}$ (CM6S4) shows the highest conductivity ($2.0\times10^{-2}$ S/cm at 700 °C) in the series as mentioned above. Therefore, the nanocomposites of CM6S4/$(Li\text{-}Na)_2CO_3$ have been prepared to further enhance the ionic conductivity at lower temperature. In addition, the effect of the carbonate content on the phase, microstructure and electrical conductivity of CM6S4/$(Li\text{-}Na)_2CO_3$ has been investigated.

### 8.2.2 Results and discussion

#### (a) Thermal analysis

Plots of DTA of all the composite samples are shown in Figs. 8.10. One endothermic (~100 °C) and one exothermic peak (~300 °C) have been observed in the DTA plots corresponding to the loss of adsorbed moisture and burning of the organic residues respectively. One broad endothermic peak is observed around 460, 466 and 479 °C for the compositions CM6S4/20LNCO, CM6S4/30LNCO and CM6S4/35LNCO respectively. This is ascribed to the melting of the carbonates. All the samples, therefore, in the system CM6S4/LNCO were calcined at 600 °C for 2 hrs.

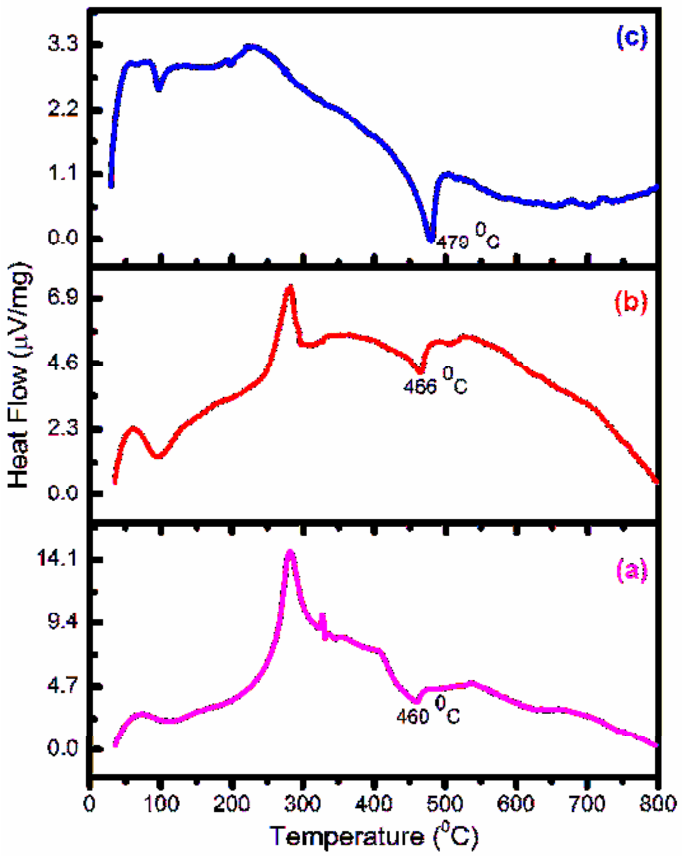

**Fig. 8.10 DTA plots of all the composite samples (a) CM6S4/20LNCO (b) CM6S4/30LNCO and (c) CM6S4/35LNCO**

### (b) Crystal structure

Powder X-ray diffraction (XRD) patterns of all the milled (uncalcined), calcined and sintered samples are recorded. Fig. 8.11 shows XRD patterns of the sintered composite samples along with CM6S4. XRD peaks have been indexed on the basis of fluorite structure similar to $CeO_2$ using JCPDS file no. 43-1002. XRD patterns do not contain any diffraction line characteristic of carbonates or any other phase. This confirms that carbonates exist as an amorphous phase in the composites. XRD patterns of the milled powders are almost the same as that of the calcined and sintered samples except that the peaks are broad in the case of milled (uncalcined) powder. Average crystallite size, D, of the milled (uncalcined) powders determined by Scherrer's formula is in the range 17-19 nm.

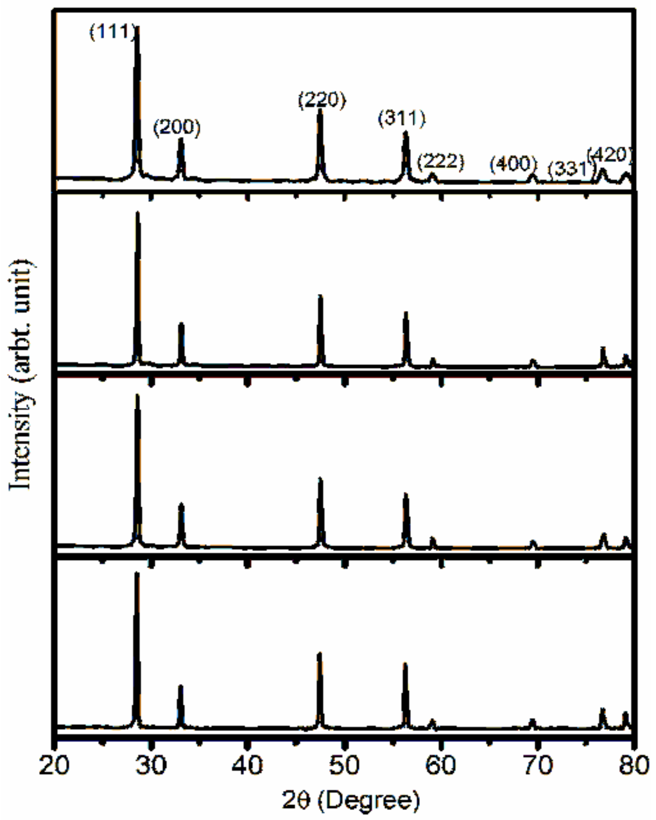

**Fig. 8.11 Powder X-ray diffraction patterns of all the sintered samples (a) CM6S4 (b) CM6S4/20 LNCO (c) CM6S4/30 LNCO and (d) CM6S4/35LNCO**

Nanosized particles have large surface area. This leads to more interaction between the two phases and hence enhances the area of interface region. Compositions CM6S4/20LNCO, CM6S4/30LNCO and CM6S4/35LNCO have density 85%, 85% and 78% of the theoretical value. This low density is due to low temperature of sintering (700 ºC). These composites, however, can still be used as electrolytes because the carbonates melt at the working temperature and serve as a seal to avoid the gas crossover and also leads to increase in the mechanical strength [Chen et al. (2010)].

### (c) Thermal expansion

Plots of thermal expansion of all the composites are given in Fig. 8.12. The plot for the composition, CM6S4/20LNCO is non linear.

Two inflection points have been observed around 673 and 773 K. Former is due to softening of the carbonate phase. At 773 K, carbonates melt completely and fill in the interspaces between the ceria particles followed by expansion again. This shows that a solid network persists in this composition even after 773 K due to insufficient amount of the liquid formed to fill all the interspaces. In the case of CM6S4/30LNCO and CM6S4/35LNCO, the thermal expansion occurs up to 723 K and then contraction occurs sharply. Compositions, CM6S4/30LNCO and CM6S4/35LNCO show nearly the same expansion behavior. Coefficient of thermal expansion of all the composites is given in Table. 8.4. It is noted from this table that coefficient of thermal expansion decreases with increasing the carbonate content. This is due to large amount of liquid formed at higher concentration filling all the pores among the ceria grains. Contraction occurs due to capillary force of the liquid among the pores.

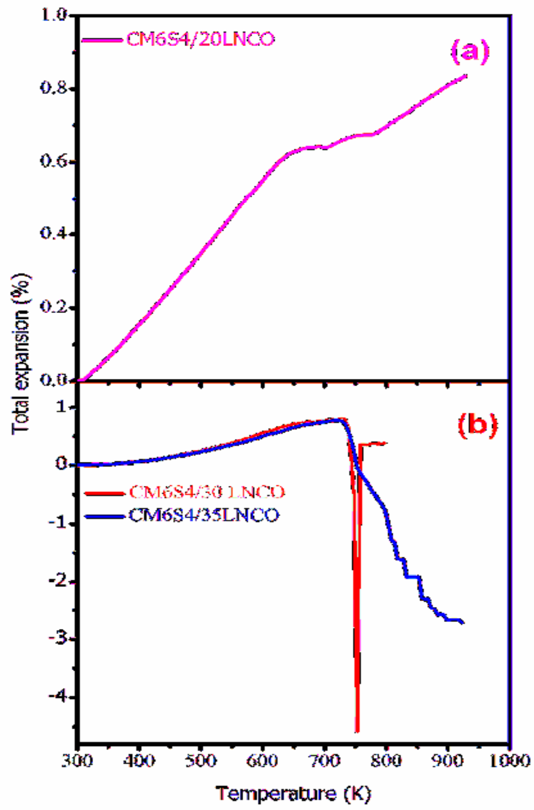

**Fig. 8.12 Thermal expansion curve of the CM6S4/LNCO nanocomposites**

**Table. 8.4 Coefficient of thermal expansion (CTE) of all the composites**

| S. No. | Compositions | CTE (/K) |
|---|---|---|
| 1. | CM6S4/20LNCO | $16.0\times10^{-6}$ |
| 2. | CM6S4/30LNCO | $11.4\times10^{-6}$<br>(300-723 K) |
| 3. | CM6S4/35LNCO | $03.0\times10^{-6}$<br>(300-723 K) |

### (d) Microstructure

Micrographs of the freshly fractured surfaces of all the sintered samples are shown in Figs. 8.13 (a)-(d). Micrograph of CM6S4 (sintered at 1350 °C for 4 hrs) is very dense.

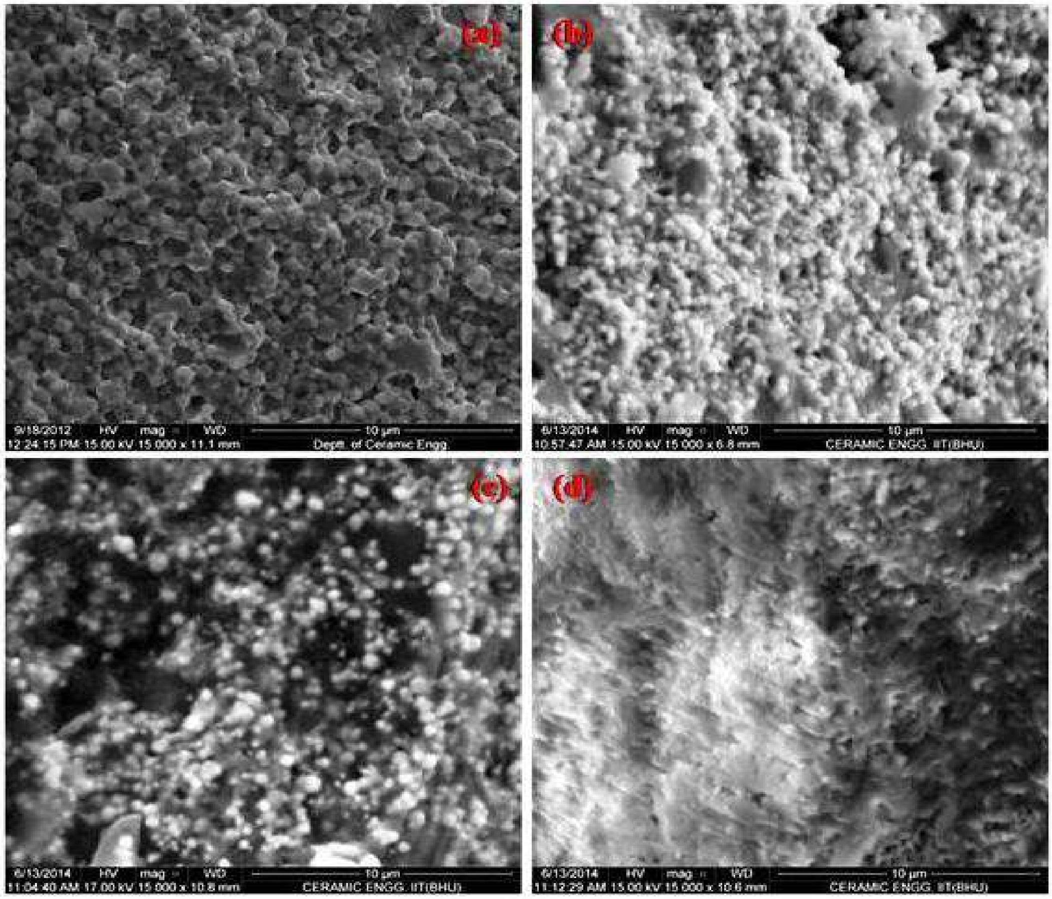

**Fig. 8.13 SEM micrographs of all the fractured surfaces of the sintered samples (a) CM6S4 (b) CM6S4/20 LNCO (c) CM6S4/30 LNCO and (d) CM6S4/35 LNCO**

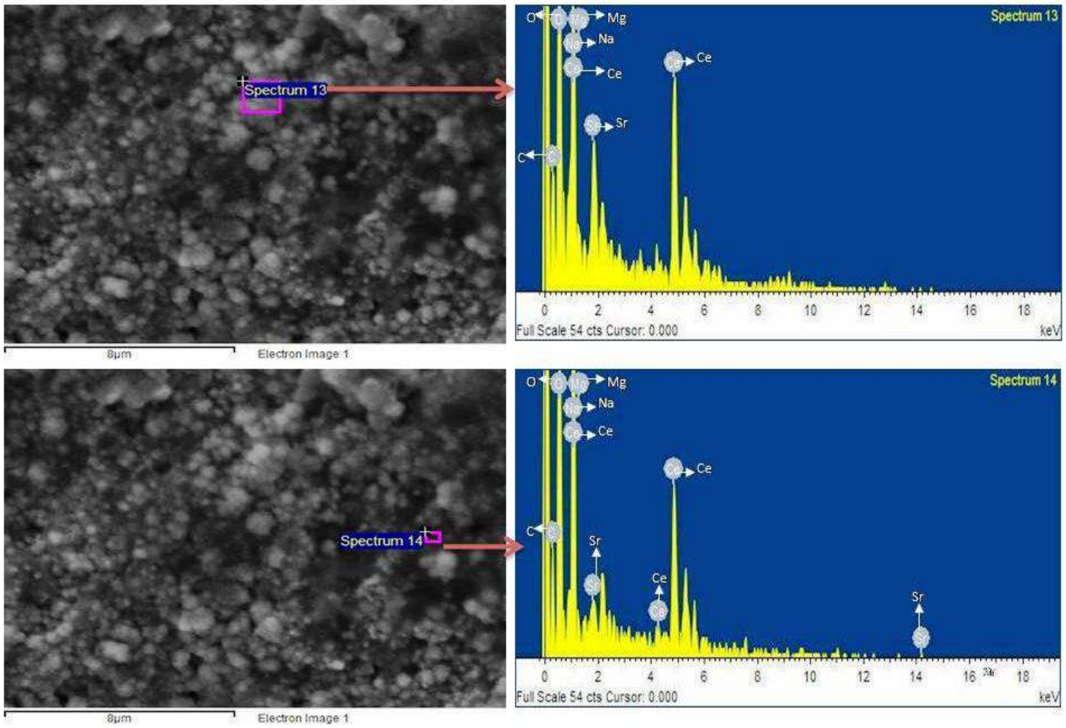

**Fig. 8.14 EDS of the composition CM6S4/35LNCO at two different points**

The composite samples have porous microstructure due to low sintering temperature (700 °C). The grains are fully covered by amorphous carbonate phase. Percolation of molten carbonate phase is obvious due to this morphology of the composites. Above the melting temperature of the carbonates, liquid fills in the interspaces among the ceria particles and serves as a seal for crossover of the gases. As the carbonates content increases, these form a continuous path around the ceria phase creating large interfacial region. Average grain size of the sintered composites samples determined using 'ImageJ' software is in the range 180-200 nm while it is 1 µm in the case of CM6S4 (sintered at 1350 °C). This is because the grain growth is inhibited by the carbonate phase.

EDS spectra of the composition CM6S4/35LNCO at two different points are given in Fig. 8.14. All the constituent elements are present in the expected stoichiometry except lithium. This shows the homogeneous distribution of ceria and carbonate phases.

### (e) Electrical conductivity

Complex plane impedance plots of all the compositions are shown in Figs. 8.15-8.17. In the case of composition, CM6S4/20LNCO, a single arc passing from the origin in the high frequency range is ascribed to contribution of the grains to the total resistance. A tail in a low frequency range corresponds to contribution of the electrode/electrolyte interface polarization. As the temperature increases, relaxation frequency of all the polarization processes increases. This leads to shifting of the arcs towards higher frequency. Above 325 °C, only the electrode arc has been observed. Above 450 °C, a tail has been observed at lower frequency side of the electrode arc. This is ascribed to a mass transfer process. It is noted from the impedance plots that a distinct arc due to the grain boundaries is absent. This shows that conduction mechanism in the dual phase ceria based nanocomposites is different from that in the co-doped ceria [Lapa et al. (2010)]. Capacitance of the grains arc is found to be in the pF ($10^{-10}$-$10^{-12}$) range [Hodge et al. (1976)]. The capacitance is determined from the relation$2\pi f_{max} RC = 1$, where $f_{max}$ is the frequency at the highest point of the arc, R is the resistance and C is the capacitance.

Similar behavior has been observed for the compositions, CM6S4/30LNCO and CM6S4/35LNCO. The intercept on the Z' axis at higher frequency side of the electrode arc has been taken as equal to the total resistance of the sample above 325 °C (when the arc due to the grains disappears). In the present investigation, only the arc of the grains (distinct grain boundaries arc is absent) is fitted to determine total resistance of the sample. Therefore, only single $R_1$-CPE1 circuit is used for fitting. The arc of the electrode is not fitted because its contribution is not considered.

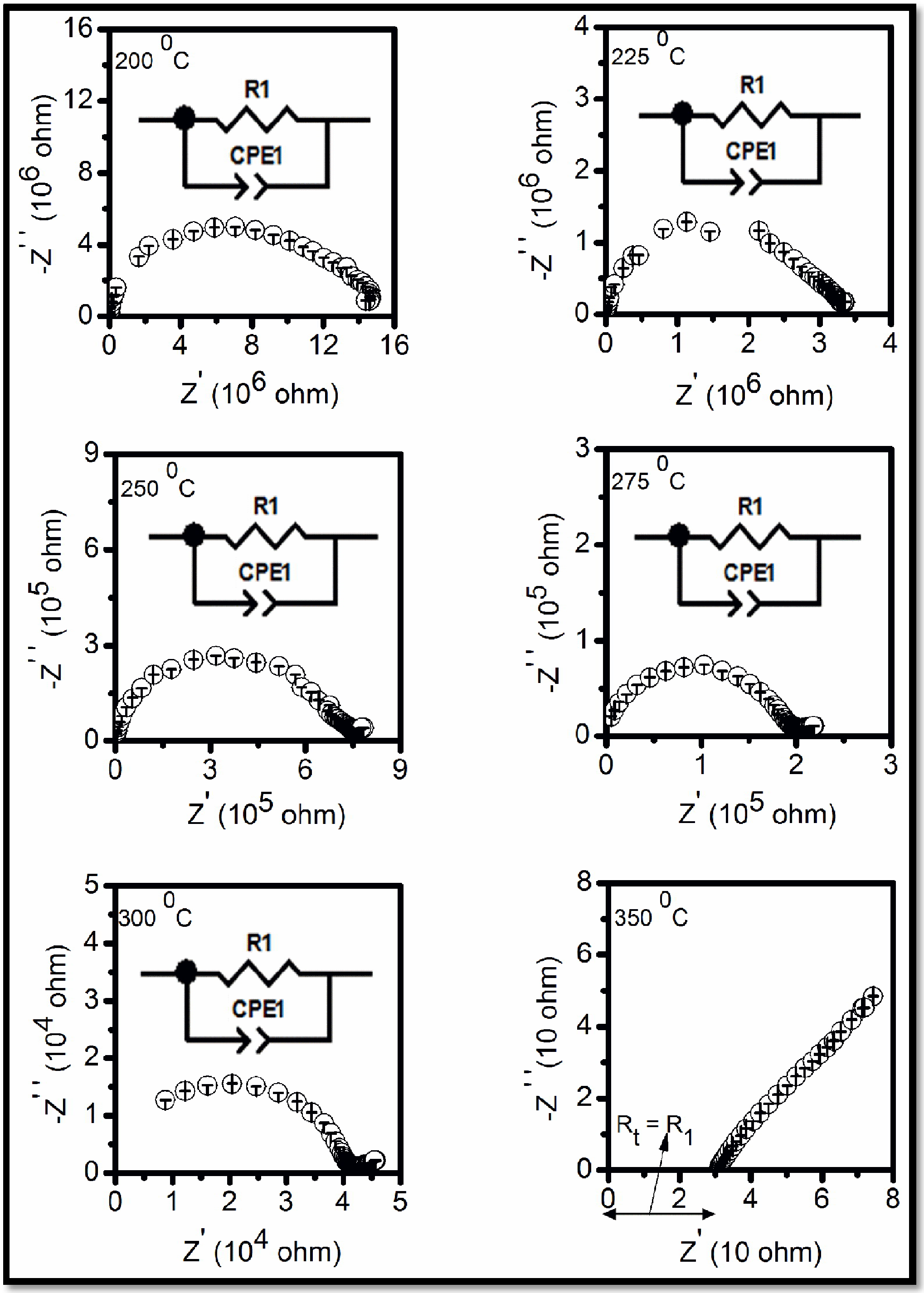

**Fig. 8.15 Complex plane impedance plots of the composition CM6S4/20LNCO at different temperatures**

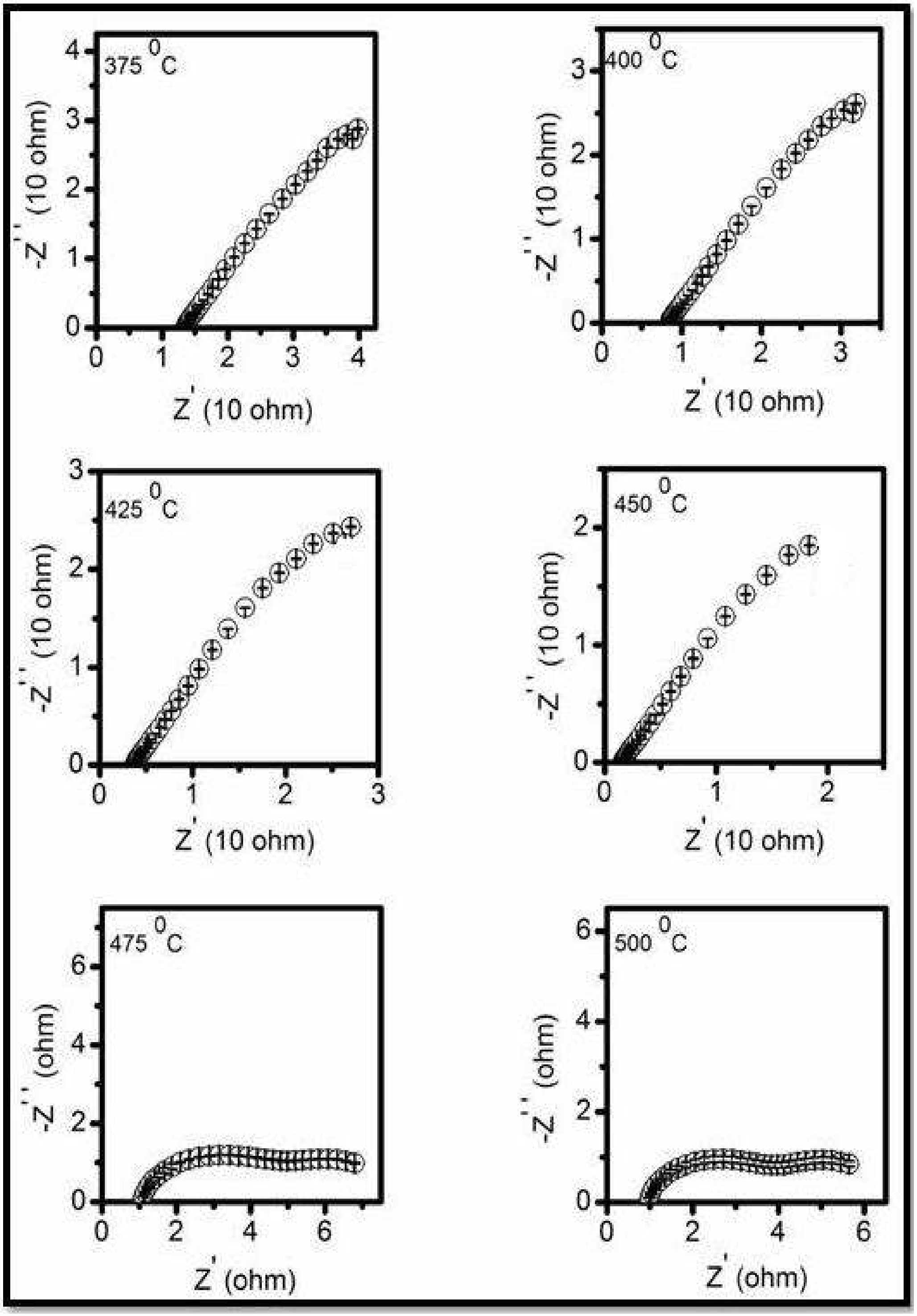

Fig. 8.15 Complex plane impedance plots of the composition CM6S4/20LNCO at different temperatures

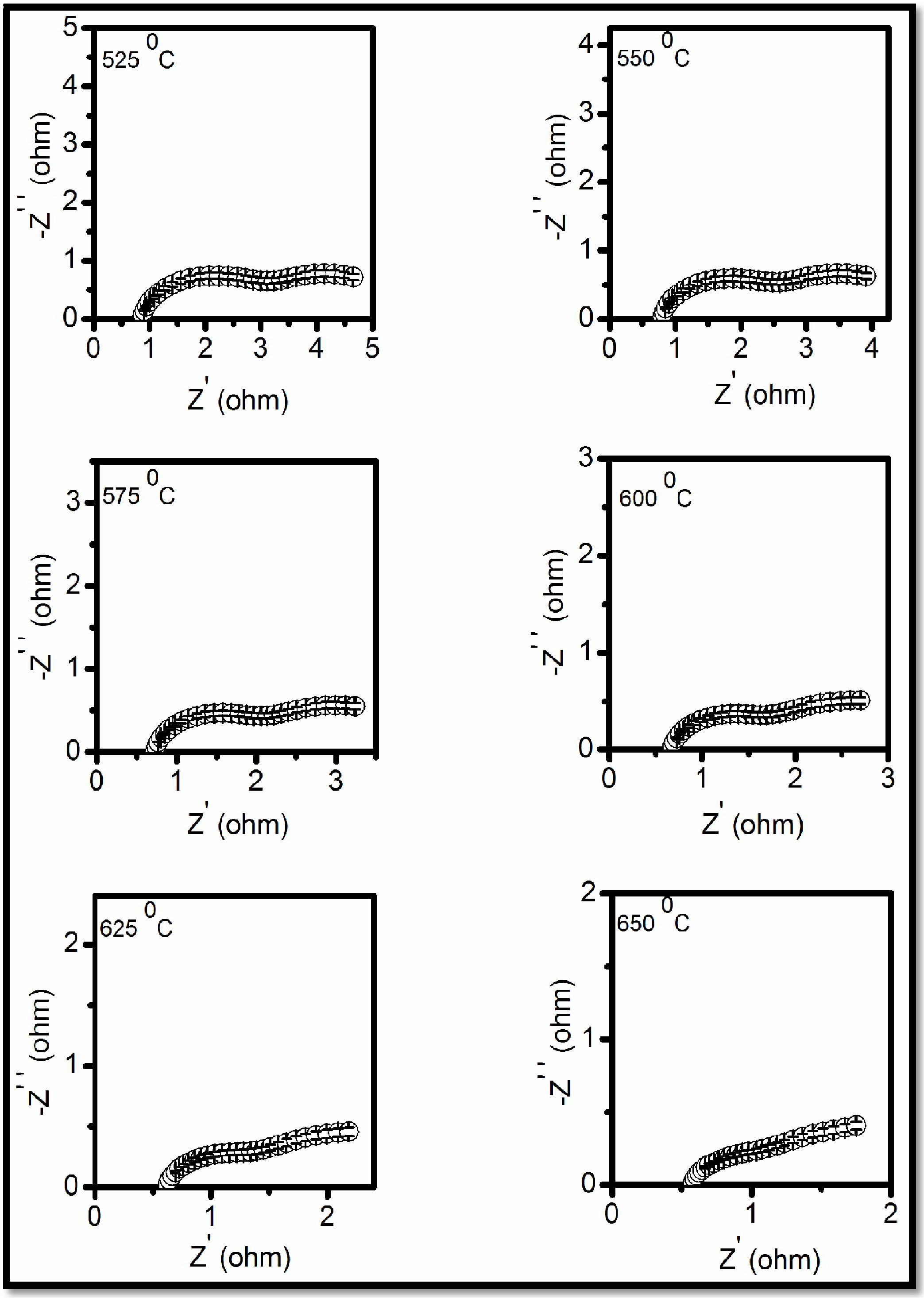

Fig. 8.15 Complex plane impedance plots of the composition CM6S4/20LNCO at different temperatures

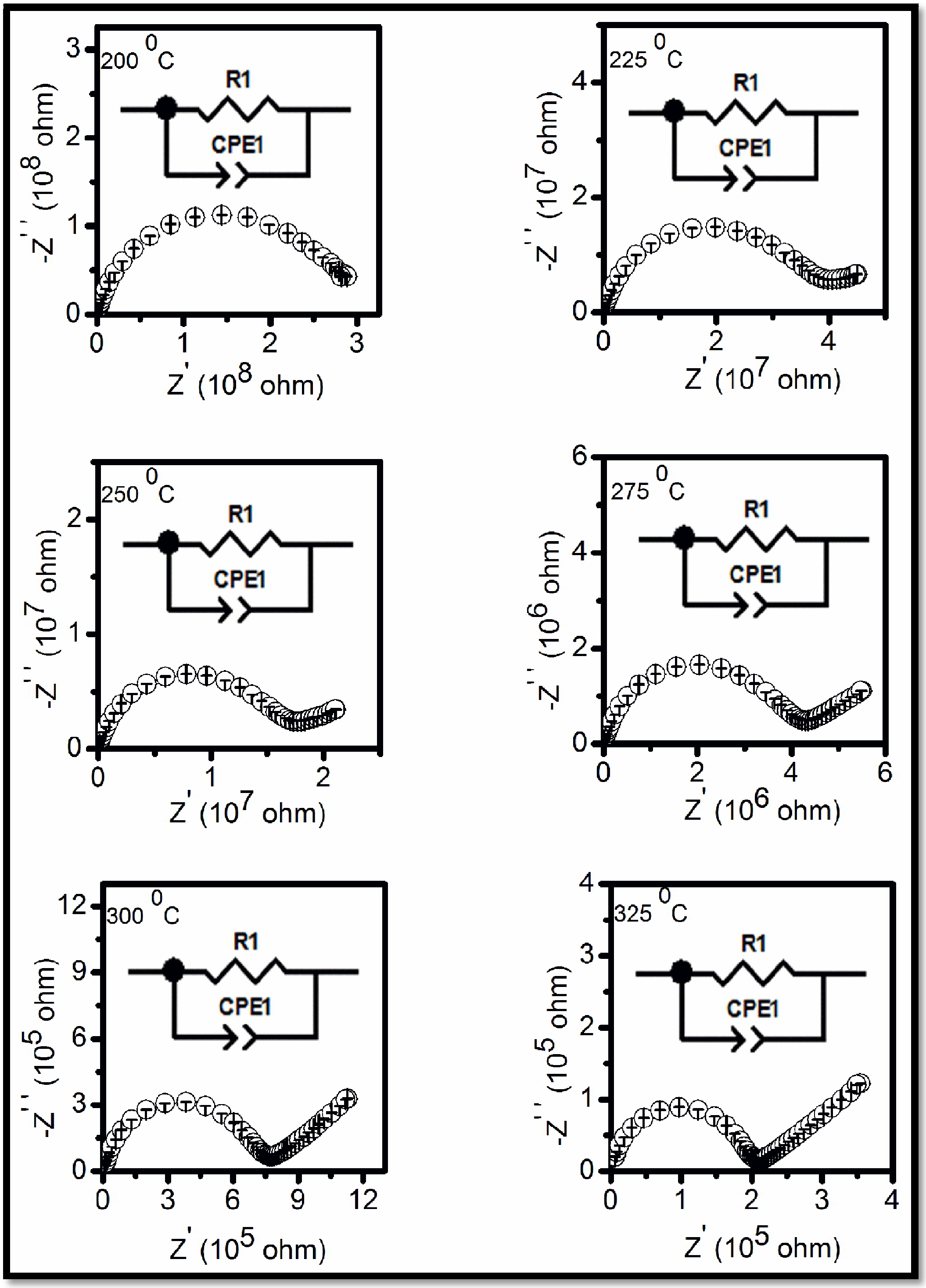

**Fig. 8.16 Complex plane impedance plots of the composition CM6S4/30LNCO at different temperatures**

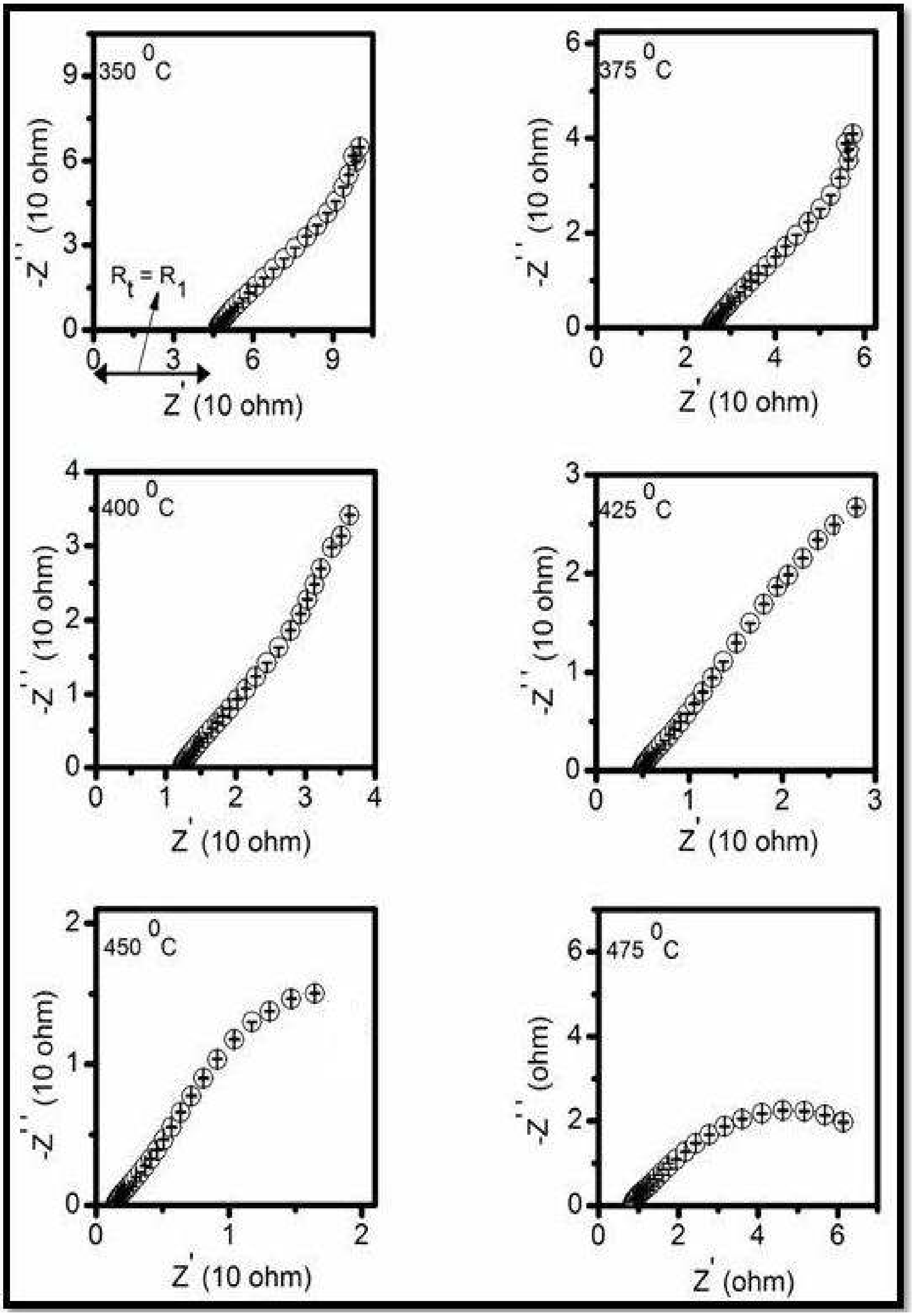

**Fig. 8.16 Complex plane impedance plots of the composition CM6S4/30LNCO at different temperatures**

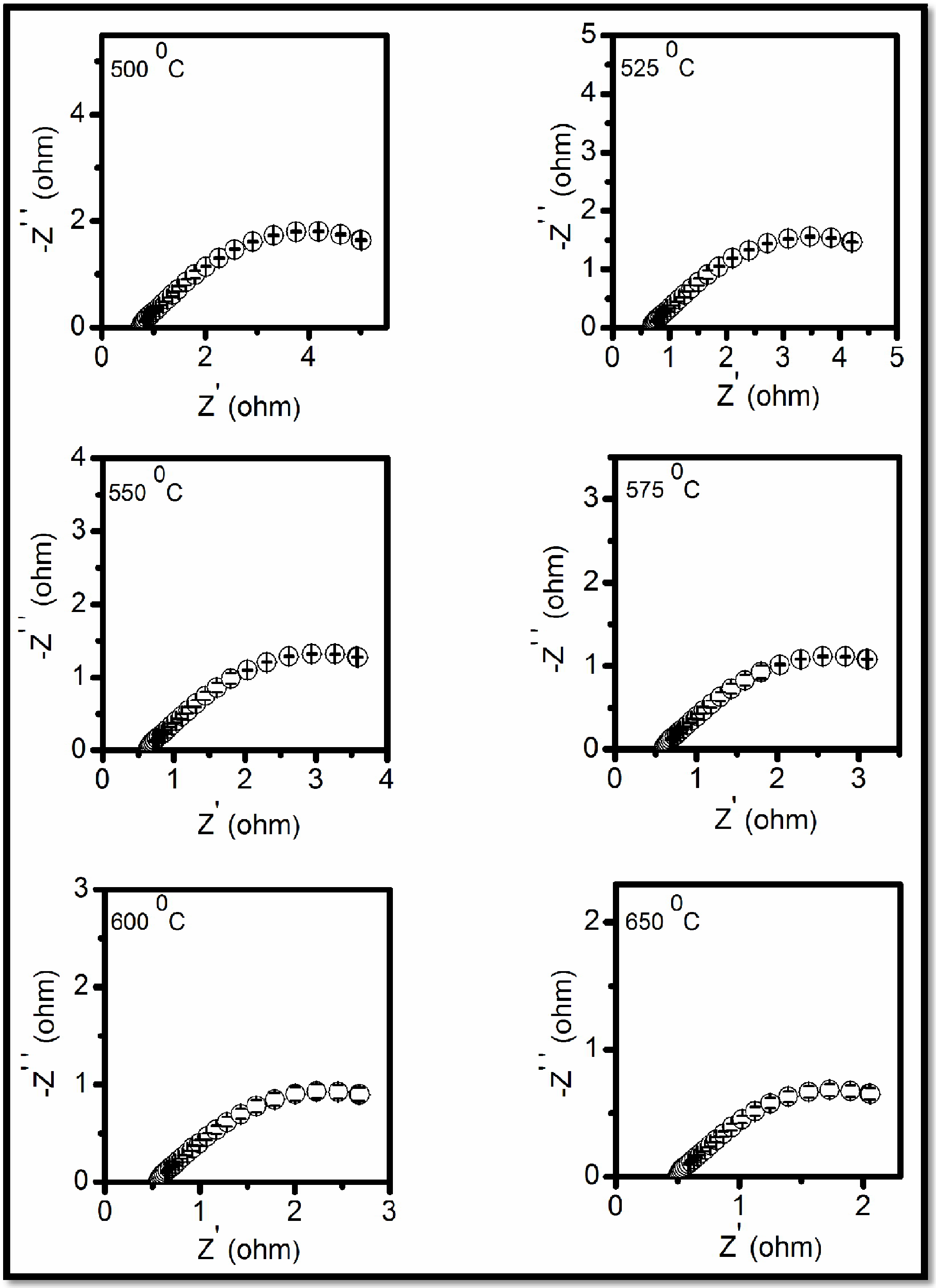

Fig. 8.16 Complex plane impedance plots of the composition CM6S4/30LNCO at different temperatures

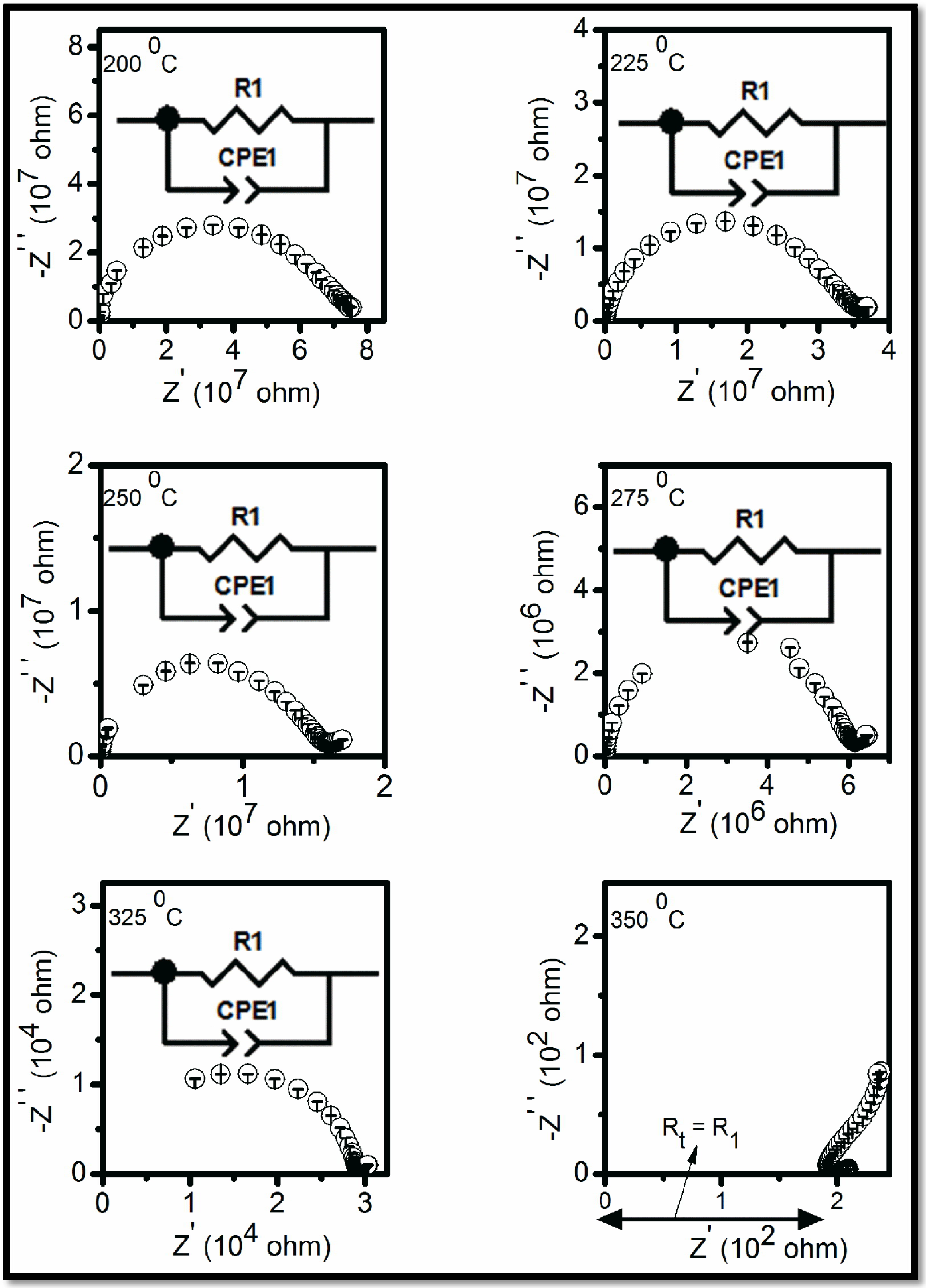

**Fig. 8.17 Complex plane impedance plots of the composition CM6S4/35LNCO at different temperatures**

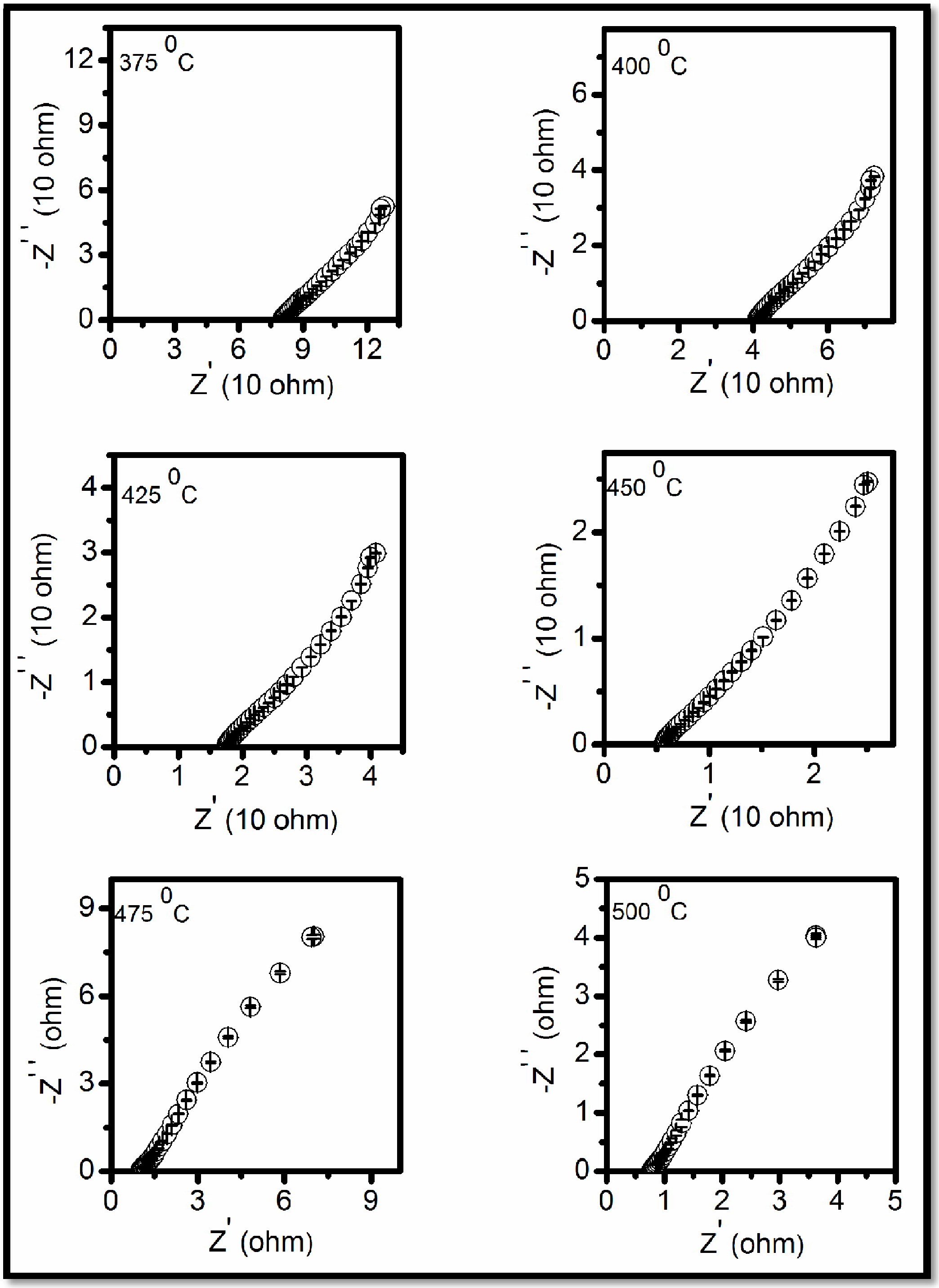

**Fig. 8.17 Complex plane impedance plots of the composition CM6S4/35LNCO at different temperatures**

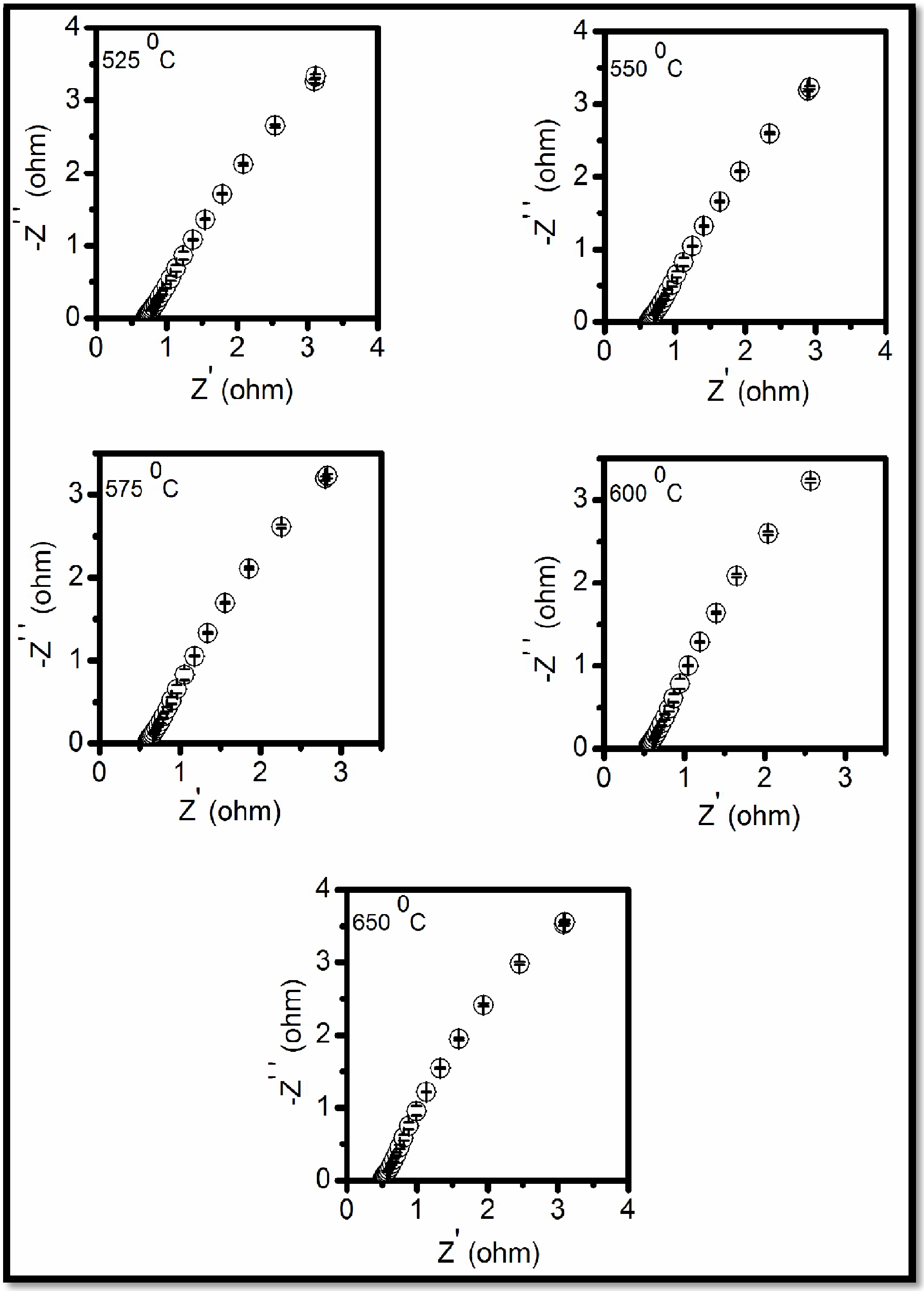

Fig. 8.17 Complex plane impedance plots of the composition CM6S4/35LNCO at different temperatures

Arrhenius plots for total ionic conductivity of all the compositions are shown in Fig. 8.18. These plots show prolonged Z-shape curve with a sharp increase in the conductivity around 350 °C. This temperature is certainly below the melting point of the carbonates, 460 °C and is called superionic transition. The lowering of the transition temperature is due to the interfacial interaction between the two phases. This leads to the threshold percolation to form a highly conducting continuous path through the interfaces below the melting temperature. Above the transition temperature, conductivity of the composites is higher than that of CM6S4 and LNCO. CM6S4/35LNCO shows the highest conductivity, 0.4 S/cm at 500 °C. Conductivity of the composites increases with increasing the carbonate content.

Below the transition temperature, conductivity of the composites is lower than that of CM6S4 due to blocking of diffusion of $O^{2-}$ ions by dispersed solid amorphous carbonate phase.

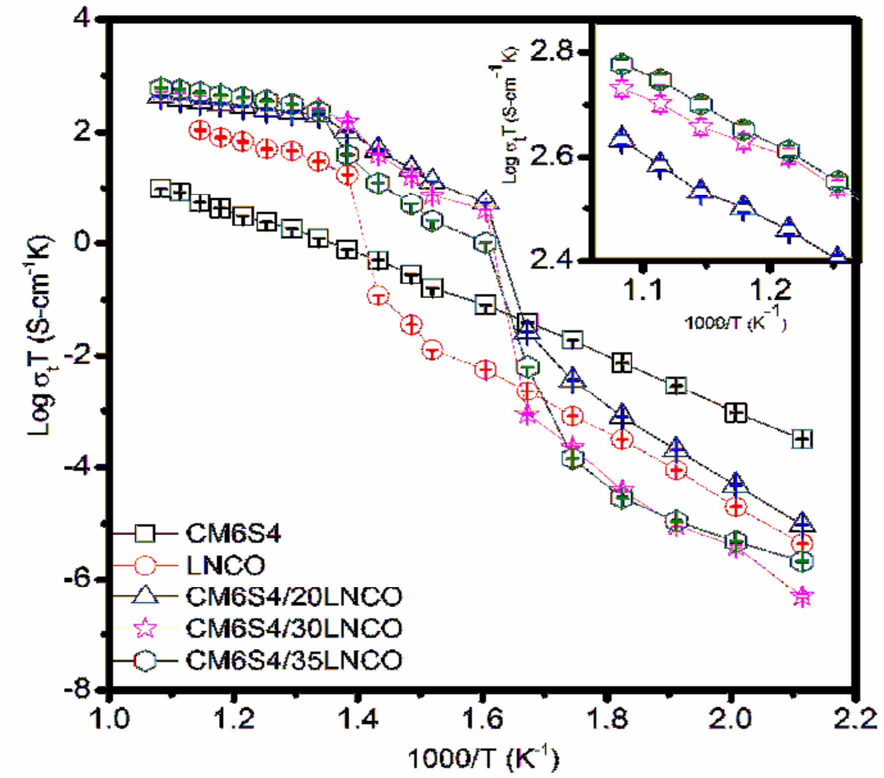

Fig. 8.18 Arrhenius plots for total ionic conductivity of all the compositions

After melting, the carbonates fill in the pores and interspaces among the ceria particles creating more interfacial region for diffusion of the ions. A space charge zone is formed at the interfaces due to interaction between the two phases. The concentration of mobile ions is higher in the space charge zone. The interfaces formed between ceria and carbonate phases in the composites have no structural limit and have large number of cationic defects than that in the bulk. Conductivity at higher temperature may have contribution from all the mobile ions such as $Na^+$, $Li^+$, $H^+$, $O^{2-}$ and $CO_3^{2-}$ leading to superionic conduction [Liu et al. (2010)].

Activation energy ($E_a$) has been determined from the slope of Arrhenius plots in the lower and higher temperature regions both. Activation energy is high in the low temperature region and low in the high temperature region. At low temperature, diffusion of the ions is restricted by the solid amorphous carbonate phase leading to high activation energy. Values of activation energy are given in Table. 8.5. Low value of activation energy (above the transition point) confirms the interfacial conduction of the ions. This is also in conformity with the value obtained by Zhu et al. (2008) for interfacial conduction of oxide ions. Values of the pre-exponential factor, $\sigma_0$ determined from the intercept of Arrhenius plots are also given in Table. 8.5.

**Table. 8.5 Total conductivity at 500 ºC, activation energy and pre-exponential factor for all the compositions**

| S. No. | Compositions | $\sigma_t$ at 500 °C (S/cm) | $E_a$ for T < 350 °C (eV) | $E_a$ forT > 350 °C (eV) | $\sigma_0$ |
|---|---|---|---|---|---|
| 1. | CM6S4 | $2.39\times10^{-3}$ | 1.12 | 0.73 | $5.49\times10^{3}$ |
| 2. | LNCO | $4.73\times10^{-2}$ | 1.26<br>(<500 °C) | 0.30<br>(>500 °C) | $3.05\times10^{6}$ |
| 3. | CM6S4/20LNCO | $2.95\times10^{-1}$ | 1.50 | 0.26 | $1.05\times10^{4}$ |
| 4. | CM6S4/30LNCO | $3.93\times10^{-1}$ | 1.61 | 0.24 | $1.20\times10^{4}$ |
| 5. | CM6S4/35LNCO | $4.00\times10^{-1}$ | 1.60 | 0.23 | $3.00\times10^{4}$ |

It is noted that composite samples have high value of $\sigma_0$ than that of CM6S4. Therefore, it is concluded that conductivity of $Mg^{2+}$ and $Sr^{2+}$ co-doped ceria/carbonate nanocomposites increases due to two reasons: (i) co-doping of $Sr^{2+}$ and $Mg^{2+}$ in ceria enhances the total conductivity as discussed in the section 1 and (ii) molten carbonates form a uniform continuous path enveloping the ceria phase. This creates highways for conduction of the ions. In nanocomposites, conduction of $O^{2-}$ ions takes place through the interfaces and in the bulk. As discussed above, conductivity can also be enhanced by increasing the value of $\sigma_0$ which depends on the concentration of mobile ions and the ion jump distance [Liu et al. (2010)]. Therefore, large number of mobile ions in the space charge zone and long jump distance at the interfaces formed between CM6S4 and LNCO results in higher ionic conductivity and low activation energy.

Variation of conductivity in the system CM6S4/LNCO with the carbonate content is given by Archie equation (discussed in detail in Chapter 4). Archie plot of the CM6S4/LNCO nanocomposites is shown in Fig. 8.19. It can be seen from Fig. 8.19 that electrical conductivity in the system CM6S4/LNCO varies linearly with the volume fraction of the molten carbonate phase in accordance with Archie equation for percolation model.

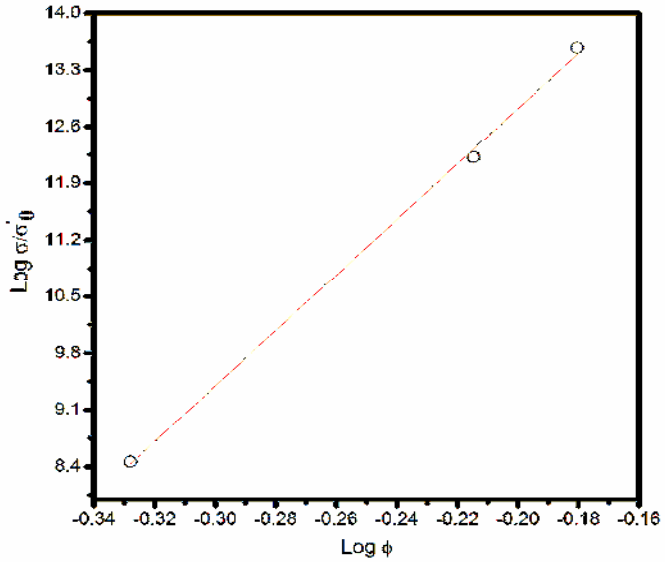

**Fig. 8.19 Arhie plot for composites in the system CM6S4/LNCO**

In the present work, the composition CM6S4/35LNCO shows conductivity, 0.4 S/cm at 500 °C which is two orders of magnitude higher than the value $2.40\times10^{-3}$ S/cm observed for CM6S4. At 450 °C this composition shows a conductivity 0.05 S/cm which is five times higher than the value 0.01 S/cm at 481 °C reported for SNDC/(Li-Na)$_2$CO$_3$ by Liu et al. (2010). Use of this composition as solid electrolyte for LT-SOFCs will reduce the cost as compared to that of SNDC/(Li-Na)$_2$CO$_3$.

### 8.2.3 Conclusion

- Nanocomposites based on CM6S4/(Li-Na)$_2$CO$_3$ have been successfully prepared by using nanocrystalline co-doped ceria powder and the binary carbonate mixture.
- Single phase formation has been confirmed by powder XRD. Carbonates are present as an amorphous phase throughout the ceria matrix. SEM micrographs show percolated islands of ceria and carbonate phases.
- Conductivity increases abruptly above the transition temperature due to increase in the number of pathways for oxygen ion conduction.
- Activation energy is very low at high temperatures. This is suggested that in the composites interfacial conduction of the ions dominates over the bulk causing low activation energy of conduction.
- The composition CM6S4/35LNCO shows the highest conductivity of 0.4 S/cm at 500 °C with an activation energy of conduction 0.30 eV.